Fuel 411 (2026) 138062

Contents lists available at ScienceDirect

Fuel

journal homepage: www.elsevier.com/locate/fuel

Full Length Article

Continuous production of γ-valerolactone from furfural using optimized catalysts containing Zr and Nb

Adrián García [a], Anna Saotta [b,c], Elianny Da Silva [a], Pablo J. Miguel [a], Alessandro Allegri [b,c], Rita Sánchez-Tovar [a], Jean-Charles Morin [d], Olivier Gardoll [d], Tomás García [e], José Manuel López [e], Stefania Albonetti [b,c,*], Nikolaos Dimitratos [b,c,*], Benjamin Solsona [a,*]

[a] Departamento de Ingeniería Química, ETSE, Universitat de València, Av. Universitat, Burjassot-Valencia 46900, Spain
[b] Dipartimento di Chimica Industriale "Toso Montanari", Alma Mater Studiorum Università di Bologna, Via Piero Gobetti 85, 40129 Bologna, Italy
[c] Center for Chemical Catalysis – C3, Alma Mater Studiorum –, Università di Bologna, Via Piero Gobetti 85, 40129 Bologna, Italy
[d] Unité de Catalyse et Chimie du Solide-UMR CNRS, Université de Lille, Villeneuve d'Ascq 59655, France
[e] Instituto de Carboquímica (CSIC), C/Miguel Luesma, Castán 4, 50018 Zaragoza, Spain

ARTICLE INFO

Keywords:
Continuous flow
Zr
Nb
Furfural, γ-Valerolactone

ABSTRACT

γ-Valerolactone (GVL) is a versatile platform molecule that can be produced from furfural (FF), a compound readily obtained from biomass. The transformation of FF into GVL can be achieved in a one-pot process through a cascade of reactions involving hydrogenation, ring opening, dehydration, and cyclization. Designing an appropriate catalyst capable of promoting all these steps in a single system is therefore essential. In this work, catalysts based on zirconium supported on Y-zeolite, as well as catalysts supported on Y-zeolite coated with a theoretical monolayer of Nb_2O_5, were synthesized and evaluated for the conversion of FF into GVL. Reactivity tests were conducted under both batch and continuous-flow conditions. The catalysts were characterized using various techniques, including XRD, FTIR, IR-Py, DR-UV–Vis, HR-TEM, XPS, and NH_3-TPD, to determine their physicochemical properties. Among the catalysts studied, Zr supported on Nb-modified Y-zeolite exhibited the highest catalytic activity, achieving a GVL yield of 65 % after 3 h at 180 °C in batch mode using 2-propanol as both hydrogen source and solvent. Similarly, under continuous-flow conditions, this bimetallic catalyst delivered the highest GVL yield (approximately 40 %), representing the best performance reported to date for this reaction. Furthermore, the addition of water to the reaction medium enhanced catalytic performance. Notably, the bimetallic catalyst maintained stable activity throughout the tested time-on-stream.

1. Introduction

The global demand for energy continues to rise due to population growth. Traditionally, this demand has been met by fossil fuels, which has led to a significant increase in greenhouse gas emissions [1–3]. To mitigate the effects of global warming caused by these emissions, alternative energy sources have been explored to replace fossil fuels [4,5]. Among these, biomass has emerged as a promising renewable resource for producing fuels and high-value chemicals, such as biofuels and solvents [6,7,8–12].

Biomass-derived compounds offer several advantages over fossil fuels, including biodegradability and biocompatibility [13,14]. Key products obtained from biomass include n-butanol, ethanol, hydroxymethylfurfural, methylfurfural, and γ-valerolactone (GVL) [15–19]. GVL has been identified as an ideal sustainable liquid for energy production and as a precursor for carbon-based chemicals such as biofuels [20,21]. Its favorable properties—safe and easy storage, colorless appearance, high boiling point, low melting point, and low toxicity—-make it an attractive compound [22–24].

GVL can be synthesized from various biomass-derived intermediates, including levulinic acid, levulinates, and furfural (FF) [25–27]. FF is an important platform molecule that can be easily obtained from biomass and is commercially produced by acid-catalyzed hydrolysis of lignocellulosic materials in aqueous media. Recent studies have focused on

* Corresponding authors.
E-mail addresses: stefania.albonetti@unibo.it (S. Albonetti), nikolaos.dimitratos@unibo.it (N. Dimitratos), benjamin.solsona@uv.es (B. Solsona).

https://doi.org/10.1016/j.fuel.2025.138062
Received 30 September 2025; Received in revised form 5 December 2025; Accepted 16 December 2025
Available online 20 December 2025

using solid acid catalysts for FF production to simplify purification processes [28–30].

The conversion of FF to GVL proceeds through a cascade reaction requiring multiple steps—hydrogenation, ring opening, dehydration, and cyclization—making catalyst design critical for achieving high GVL yields while minimizing humin formation and undesired by-products [31,32]. An effective catalyst must provide the appropriate type and strength of acid sites to promote all steps in the cascade.

Heterogeneous catalysts have been widely studied for this purpose, often involving metals supported on various materials to enhance the number and reactivity of active sites. Recent research has explored heteropolyacid-based materials with promising results [33,34]. Among the metals investigated, zirconium has been the most widely employed due to its superior selectivity toward GVL (Table S1) [32,35–38], particularly when combined with acids or supported on zeolites [39–41]. Zeolites are attractive supports because they provide Brønsted acid sites (BAS), while ZrOx contributes Lewis acid sites (LAS). Both types of sites are essential for the one-pot FF-to-GVL transformation, as they participate in different steps of the cascade [42]. However, the BAS/LAS ratio must be carefully tuned to maximize GVL selectivity and minimize by-product formation [16,43,44].

Niobium, although less studied for this reaction, exhibits acidic properties that could be advantageous. Moreover, Nb combined with noble metals such as Ru has been shown to enhance levulinic acid hydrogenation to GVL [45].

The FF-to-GVL reaction involves two hydrogenation steps, requiring an appropriate hydrogen source. Alcohols are commonly used because they serve as both solvent and hydrogen donor [46]. The hydrogen transfer occurs via the Meerwein–Ponndorf–Verley (MPV) mechanism, an attractive alternative to molecular hydrogen [47,48]. Among alcohols, 2-propanol is often considered the most selective for GVL formation [44,47,49–51].

Most studies on FF-to-GVL conversion have been conducted in batch reactors. However, continuous-flow processing offers significant advantages, including improved mass and heat transfer, reduced residence times, simplified downstream operations, enhanced scalability, and higher reactor productivity. Despite these benefits, continuous-flow studies remain scarce, and reported GVL yields have been modest. Previous works [52,53] have explored Zr-based catalysts, sometimes combined with metals such as Pt or Ti, but mainly yielded intermediates like furfuryl alcohol (FAL) and furfuryl ether (FE), with GVL yields below 20 %.

Considering the favorable catalytic properties of Zr and the potential promoting effect of Nb, this study proposes the synthesis of Zr catalysts supported on Nb-modified Y-zeolite. Catalytic performance was evaluated under both batch and continuous-flow conditions. The results demonstrate that the GVL yields achieved here surpass the highest values previously reported under continuous-flow operation. Furthermore, structure–activity relationships were elucidated through comprehensive characterization and mechanistic insights.

2. Materials and methods

2.1. Reagents

The synthesis of the catalysts was carried out using zirconium (IV) oxynitrate hydrate ($ZrO(NO_3)_2{\cdot}xH_2O$ (99 % purity) from Sigma-Aldrich, St. Louis, MO, USA), ammonium niobiate (V) oxalate hydrate ($C_4H_4NNbO_9{\cdot\cdot}H_2O$) (99 % purity) from Sigma-Aldrich, St. Louis, MO, USA), zeolite Y (Si/Al = 15 at. ratio, 100 % purity from Zeolyst International, Conshohocken, PA, USA). The substrate used for the reaction was furfural (99 % purity) and the solvent was 2-propanol (99.5 % purity) from Sigma-Aldrich, St. Louis, MO, USA.

2.2. Synthesis of catalysts

A Zr monometallic catalyst was synthesized by the wet impregnation method using deionized water. Specifically, 0.19 g of zirconium(IV) oxynitrate hydrate was dissolved in 20 mL of deionized water. Once the precursor was completely dissolved, 1 g of Y-zeolite was added to the solution, and the mixture was heated under stirring on a hot plate until most of the solvent had evaporated. The resulting paste was dried overnight in an oven at 120 °C and subsequently calcined in static air at 500 °C for 6 h. The final zirconium oxide loading was 10 wt%, corresponding to the optimal value reported in the literature [54]. This catalyst was designated as Zr/Al-HY.

A Nb monometallic catalyst supported on Y-zeolite, with a Nb loading corresponding to a theoretical monolayer (5.8 Nb atoms nm^{-2}) [55,56], was also prepared by wet impregnation. For this synthesis, 2.28 g of ammonium niobate(V) oxalate hydrate was dissolved in 20 mL of deionized water. After complete dissolution, the zeolite was added, and the mixture was stirred on a hot plate until nearly all the solvent had evaporated. The paste was dried overnight at 120 °C and calcined at 500 °C in static air for 6 h. This catalyst was labeled as (Nb)Al-HY.

Finally, Zr was deposited onto the (Nb)Al-HY sample (zeolite coated with a theoretical Nb_2O_5 monolayer) using the same wet impregnation procedure, followed by drying at 120 °C overnight and calcination at 500 °C for 6 h. This bimetallic catalyst was designated as 10Zr/(Nb)Al-HY.

2.3. Characterization techniques

The fresh and used catalysts were characterized using various techniques to determine their physicochemical properties and establish structure–activity relationships.

Textural parameters (Specific Surface Area BET, Volume of pores and Diameter of pores) were assessed via N_2 adsorption–desorption porosimetry using a Microtrac MRB BELSORP MINI X. Prior to cooling in a liquid nitrogen bath for N_2 adsorption, samples were outgassed at 150 ∘C. Surface areas were determined by using the Brunauer–Emmett–-Teller (BET) equation assuming a cross section of 0.162 nm^2 for the nitrogen molecule. The pore size distribution was obtained using the Barrett–Joyner–Halenda (BJH) model.

Powder X-ray diffraction (XRD) patterns were recorded in the 2θ range of 10°–80° using an Enraf Nonius FR590 sealed-tube diffractometer (Bruker, Delft, The Netherlands) equipped with a monochromatic Cu $K\alpha_1$ source (30 mA, 40 kV).

High-resolution transmission electron microscopy (HR-TEM) was employed to examine catalyst morphology and structure using a TECNAI G2 F20 microscope (FEI Company, Hillsboro, OR, USA) operating at 200 kV and a JEM 3000F microscope (JEOL, Tokyo, Japan) at 300 kV. HR-TEM was also used for energy-dispersive X-ray spectroscopy (EDX) and selected-area electron diffraction (SAED). Prior to analysis, samples were sonicated in ethanol for 20 min and deposited on a holey carbon film supported on a copper grid.

Diffuse reflectance UV–Vis spectroscopy (DR-UV–Vis) was performed using a Shimadzu UV-2600 spectrophotometer equipped with a Harrick "Praying Mantis" diffuse reflection accessory. Fourier-transform infrared spectroscopy (FTIR) was carried out on a Cary 600 spectrometer (Agilent Technologies) with a resolution of 4 cm^{-1} and a scanning frequency of 32 min^{-1}, collecting spectra in the 4000–500 cm^{-1} range.

X-ray photoelectron spectroscopy (XPS) was conducted using a Kratos Axis Ultra DLD spectrometer with a non-monochromatized Mg Kα X-ray source ($h\nu = 1253.6$ eV). Survey scans were recorded at a pass energy of 50 eV, and high-resolution scans at 20 eV. Binding energies were referenced to the C 1 s peak at 284.8 eV from adventitious carbon. Data analysis was performed using CasaXPS software (version 2.3.15).

NH_3-temperature-programmed desorption (NH_3-TPD) was carried out on a Micromeritics Autochem II 2920 instrument equipped with a U-shaped quartz reactor. Approximately 100 mg of catalyst was pretreated

at 500 °C (10 °C min^{-1}) under an argon flow (50 mL min^{-1}). After cooling to 100 °C, NH_3 adsorption was performed using a 10 % NH_3/Ar mixture (30 mL min^{-1}) for 30 min, followed by purging with Ar (50 mL min^{-1}) for 2 h to remove physisorbed NH_3. Desorption was then carried out by heating to 800 °C at 10 °C min^{-1} under Ar (30 mL min^{-1}). The amount of desorbed NH_3 was quantified using a Pfeiffer Vacuum GSD 350 mass spectrometer ($m/z = 17$), calibrated with NH_3 injections and corrected for water interference.

Pyridine adsorption–desorption IR spectroscopy (IR-Py) was used to distinguish Brønsted and Lewis acid sites. Samples were pressed into self-supporting wafers (5 mg cm^{-2}), pretreated at 723 K under high vacuum (10^{-6} mbar) for 2 h, and exposed to pyridine vapor. Spectra were normalized to a 10 mg wafer. Acid site concentrations were calculated using the bands at 1545 cm^{-1} (Brønsted, $\varepsilon B = 1.67$ cm μmol^{-1}) and 1455 cm^{-1} (Lewis, $\varepsilon L = 2.22$ cm μmol^{-1}) [57,58].

Thermogravimetric analysis (TGA) was performed on fresh and used catalysts using a TGA550 instrument (TA Instruments). The heating program consisted of a ramp to 150 °C at 10 °C min^{-1}, an isotherm for 15 min, followed by heating to 700 °C at 10 °C min^{-1} with a 5 min isotherm, under an air flow.

2.4. Catalytic test and analysis in batch reactors

Catalytic Testing in Batch Mode.

The catalytic conversion of furfural (FF) to γ-valerolactone (GVL) was performed in a 25 mL Teflon-lined stainless-steel autoclave reactor. The reactor was charged with 5 mL of a 0.025 M (25 mM) FF solution in 2-propanol and 0.1 g of catalyst. Before sealing, the reactor was purged three times with N_2 to remove air. The reaction was carried out in a silicon oil bath at 180 °C under continuous stirring (800 rpm) for the desired time. After the reaction, the autoclave was cooled in an ice bath, and the liquid phase was recovered by filtration for quantitative analysis.

Product Analysis.

Reaction products were analyzed by gas chromatography (GC) using dodecane as an external standard. Quantitative analysis was performed on an HP5890 GC instrument (Hewlett-Packard, Palo Alto, CA, USA) equipped with an Agilent HP-1 capillary column (30 m × 0.32 mm × 0.25 μm), an injection port at 220 °C, and a flame ionization detector (FID) at 240 °C. The temperature program was as follows: (i) isothermal at 35 °C for 30 min, (ii) heating at 1.5 °C min^{-1} from 35 °C to 230 °C, and (iii) isothermal at 230 °C for 30 min.

For product identification, a GC–MS system (Agilent 7890A GC coupled with 5977A MSD, Santa Clara, CA, USA) was employed using the same temperature program as for GC-FID analysis.

2.5. Catalytic test and analysis in continuous flow reactors

Continuous flow reactions were performed using a homemade liquid-phase fixed-bed reactor [52]. A HPLC pump (JASCO PU4080i) feeds the solution to a reactor placed in an oven. There is a VCR filter at the exit of the reactor, followed by a backpressure regulator (BPR). The diluent was silicon carbide (SiC) and it was added to the reactor along with 1 mL (*ca.* 0.5 g) of catalyst. It was positioned inside the oven's isothermal zone.

The contact time (τ) in continuous flow settings is the amount of time the catalyst and the reagent solution are in contact with each other. It is calculated by considering the catalyst volume (V) and the volumetric flow rate (f). In this work, the contact time is expressed in minutes as follows:

$$\tau\,(min) = \frac{V(mL)}{f\left(\frac{mL}{min}\right)}$$

Catalytic Testing in Continuous Flow

To facilitate catalyst separation at the end of the reaction, both catalysts and diluent were sieved prior to use. Catalysts were shaped into pellets with particle sizes between 177–250 μm (mesh size 60/80), while the diluent had a particle size larger than 60 mesh. The particle size was selected based on heuristic guidelines, which recommend that catalyst particles in continuous-flow systems should have a diameter approximately one-tenth of the reactor's inner diameter. This criterion minimizes pressure drop, maximizes liquid–solid contact, and prevents channeling.

All tests were conducted at a constant liquid hourly space velocity (LHSV) of 6 h^{-1}, corresponding to a volumetric flow rate of 6 mL h^{-1} and a reactor volume of 1 mL. Following the procedure described in previous work [52], the reactor was pressurized with N_2 and filled with the substrate solution before heating to stabilize pressure and flow. Once the oven reached the desired temperature, liquid samples were collected periodically from the reactor outlet.

The feed solution consisted of 67 mM furfural in 2-propanol, prepared in a 250 mL flask. Collected samples were diluted with 2-propanol and analyzed by gas chromatography (Shimadzu GC-2010 Pro) equipped with a flame ionization detector (FID). The analysis conditions were as follows: (i) injector temperature: 250 °C for complete vaporization of the mixture, using helium as the carrier gas (1.2 mL min^{-1}) and a split ratio of 30:1; (ii) column: Agilent HP-5 (30 m × 0.32 mm); oven program: 50 °C isothermal for 2 min, ramp at 10 °C min^{-1} to 250 °C, followed by 2 min isothermal at 250 °C; (iii) detector: FID at 250 °C.

Fig. S1 shows the chromatogram depicting the signals of the standard used, of all the calibrated species and of those obtained from the reactions carried out, at their respective retention times. In order to obtain the moles of the various compounds actually present at the end of the reaction, it is necessary to calibrate the instrument. Calibrations were carried out on the individual compounds (see detailed info in Tables S2 and S3).

3. Results

3.1. Characterization results

Catalysts consisting of Zr supported on Al-HY zeolite (Zr/Al-HY) and on a monolayer of Nb_2O_5 over Al-HY zeolite (Zr/(Nb)-Al-HY) were synthesized, characterized, and their catalytic performances compared.

First, the catalysts and the zeolitic support (Al-HY) were analyzed by N_2 adsorption–desorption to determine their surface areas and pore size distribution.

As shown in Table 1, the Al-HY zeolite exhibited a surface area of 819 $m^2\,g^{-1}$, which decreased upon metal incorporation, depending on the metal loading. The surface area of 10Zr/Al-HY was slightly lower (724 $m^2\,g^{-1}$), whereas the addition of a Nb monolayer caused a significant reduction (412 $m^2\,g^{-1}$). A further decrease was observed for the bimetallic 10Zr/(Nb)Al-HY catalyst (366 $m^2\,g^{-1}$).

Regarding the isotherm curves, they can be classified as type IV with H4 hysteresis, typical of mesoporous materials (Fig. 1a). The observed hysteresis loop arises from pore blocking and capillary condensation, commonly associated with bottleneck-type pores that narrow and widen along their length. All samples exhibit a relatively high N_2 uptake at low relative pressure, indicating a small average mesopore diameter. This is

Table 1
BET specific surface area ($m^2 \cdot g^{-1}$) and TPD-ammonia results for the catalysts and bare support.

Catalyst	Surface area ($m^2\,g^{-1}$)	Acid sites per g ($mmol_{NH3}\,g^{-1}$)	Acid sites density ($\mu mol_{NH3}\,m^{-2}$)	T_{max} desorption NH_3 (°C)
Al-HY	819	0.75	0.090	397
10Zr/Al-HY	724	0.72	0.099	359
(Nb)Al-HY	412	0.49	0.105	246
10Zr/(Nb) Al-HY	366	0.43	0.141	224

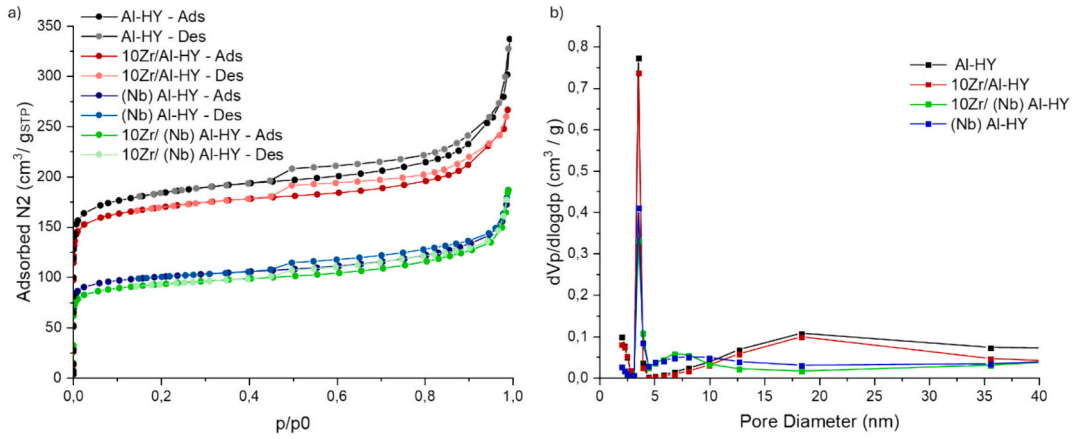

Fig. 1. Comparison of N_2 adsorption–desorption isotherms for Zr/Nb based catalysts (a) and their pore size distribution (b).

confirmed by Fig. 1b, where each sample displays a high peak between 2 and 5 nm, indicating a rather high pore distribution in between this range. A second, broader pore-size distribution peak is also present for all materials, although its position varies: Al-HY and 10Zr/Al-HY show a maximum around 17 nm, whereas (Nb)Al-HY and 10Zr/(Nb)Al-HY show a maximum near 7 nm. This difference is likely caused by the Nb monolayer partially covering the larger pores. Such pore coverage also results in lower N_2 adsorption capacity for the latter two samples, as seen in Fig. 1a.

The acidity of the support and catalysts was assessed by NH_3-TPD (Table 1 and Fig. 2a–b). This technique also provides information on acid strength (Fig. 2b): based on NH_3 desorption temperatures, acid sites can be classified as weak (<200 °C), medium (200–400 °C), and strong (>400 °C) [59,60]. The bare zeolite exhibited a TPD profile with two main desorption peaks, reflecting the presence of acid sites of different strengths; as shown in Fig. 2b, it is predominantly characterized by medium and strong acidity. Introducing Zr (10Zr/Al-HY) did not substantially change either the total acidity or the distribution of acid strengths (0.72 mmol NH_3 $g^{-}1$ and 359 °C, respectively) respect to the pure zeolite (0.75 mmol NH_3 $g^{-}1$ and 397 °C). In contrast, deposition of a Nb monolayer markedly reduced both total acidity and acid strength (0.49 mmol NH_3 $g^{-}1$ and 246 °C). Adding Zr to the Nb-modified sample led to a further decrease (0.43 mmol NH_3 $g^{-}1$ and 224 °C), likely due to partial coverage of the zeolite's acid sites by zirconium species. Although the 10Zr/(Nb)Al-HY catalyst exhibited the lowest acid site concentration per gram (Table 1), its acid site density normalized by surface area (0.141 μmol NH_3 $m^{-}2$) was higher than that of (Nb)Al-HY (0.105 μmol NH_3 $m^{-}2$). These results indicate that Zr incorporation has minimal impact on the acidity of the zeolite, whereas Nb significantly modifies its acidic properties.

FTIR-pyridine adsorption–desorption was employed to quantify and differentiate Lewis (LAS) and Brønsted (BAS) acid sites (Fig. 3a). The absorption band at 1455 cm^{-1} corresponds to pyridine coordinated to LAS [57,61]. When Nb was present, this band shifted slightly toward higher frequencies (from 1455 to ~ 1448 cm^{-1}), likely due to structural modifications of the support induced by Nb deposition. The band at 1545 cm^{-1} is attributed to pyridinium ions adsorbed on BAS, while the band at 1492 cm^{-1} indicates pyridine interacting with both LAS and BAS [57,61].

Quantitative results (Table 2) show that the bare zeolite and the Zr-containing sample exhibited the highest total acidity, primarily due to their greater Brønsted acidity compared to Nb-containing samples. However, the bimetallic catalyst displayed the highest Lewis acidity among all materials. The calculated BAS/LAS ratios followed the same trend as total acidity: Al-HY and 10Zr/Al-HY had the highest ratios, followed by the bimetallic catalyst, and finally (Nb)Al-HY. These findings suggest that Nb deposition significantly reduces the number of accessible acid sites, resulting in the lowest total acidity. This observation is consistent with NH_3-TPD results (acid site density, μmol NH_3 m^{-2}).

FTIR-Py analysis also provided insights into acid strength (Fig. 3b). Based on pyridine desorption temperatures, acid sites were classified as

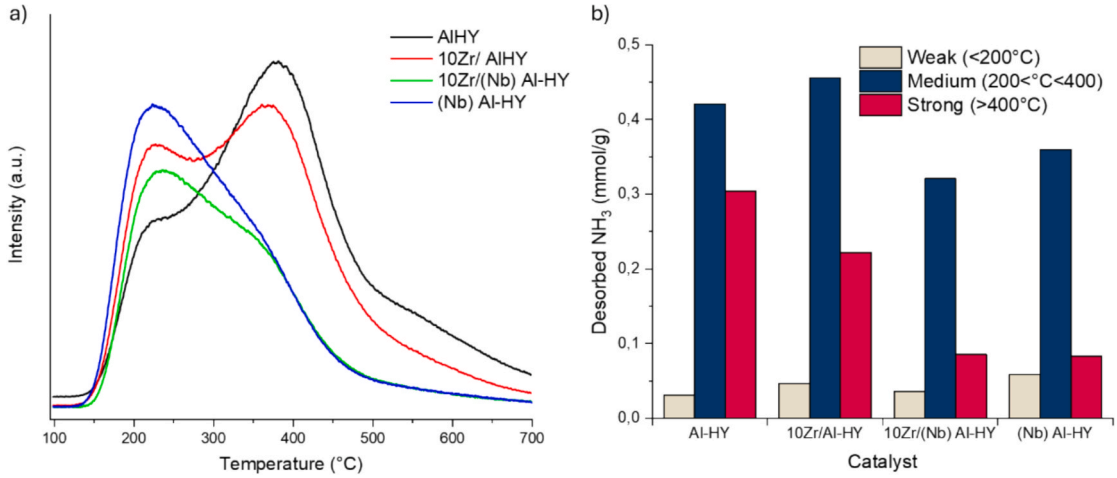

Fig. 2. TPD-NH_3 profiles of the catalysts and the support (a) and density of acid sites with different strength (weak, medium and strong) for the catalysts and support (b).

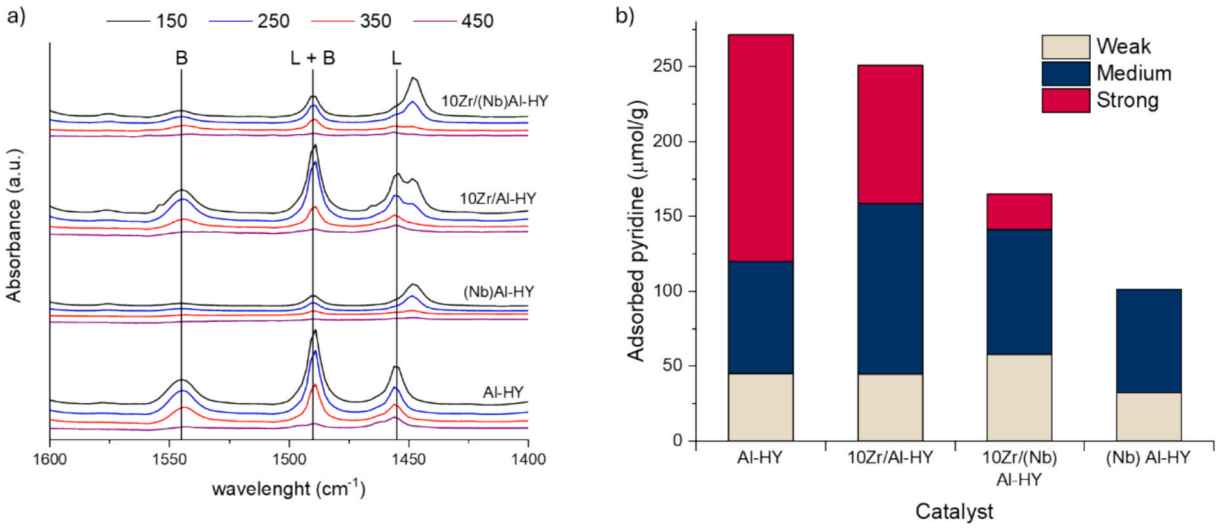

Fig. 3. FTIR spectra of adsorbed pyridine at different temperatures for the different catalysts (b); total acidity obtained by pyridine adsorption and density of acid sites with different strength (weak, medium and strong) for the catalysts and support (b).

Table 2
Acid total sites density ($\mu mol_{py}\ g^{-1}$), Lewis and Brønsted acid sites density ($\mu mol_{py}\ g^{-1}$) and BAS/LAS ratio obtained via FTIR with pyridine.

Catalyst	Acid sites ($\mu mol_{py}\ g^{-1}$)	LAS ($\mu mol_{py}\ g^{-1}$)	BAS ($\mu mol_{py}\ g^{-1}$)	BAS/LAS ratio
Al-HY	271.4	113.0	158.4	1.40
10Zr/Al-HY	250.97	103.5	147.4	1.42
(Nb)Al-HY	101.2	86.4	14.8	0.17
10Zr/(Nb)Al-HY	165.2	131.5	33.7	0.26

weak (150 °C), medium (250 °C), and strong (350 °C), with pyridine typically desorbed completely by 450 °C. The support exhibited the highest total acidity and the greatest density of strong acid sites. Metal deposition reduced both total acidity and strong site density, particularly in the presence of Nb, where strong acid sites were completely absent. These results are also in line with those obtained through NH_3-TPD analysis.

The crystalline structure of the catalysts and support was analyzed by X-ray diffraction (XRD) to assess the preservation of the zeolite framework and the dispersion of metal species. Fig. 4a shows the XRD patterns of the samples. All materials exhibited the characteristic diffraction peaks of Y-zeolite in the 2θ range of 6°–32° (2θ = 6, 10, 12, 16, 19, 20, 24, 27, 31, and 32°), confirming that the zeolite structure remained intact after metal incorporation [51,62,63]. No diffraction peaks corresponding to crystalline ZrO_2 (2θ = 17.5, 24.1, 28.1, 30.2, 31.6, 34.2, 34.6, 40.6, 50.3, 51.0, 60.0°) [53] or Nb_2O_5 (2θ = 22.5, 28.3, 36.5, 46.1, 50.9°) [64] were detected, indicating that Zr and Nb species were highly dispersed on the support.

Diffuse reflectance UV–Vis spectra of the catalysts are shown in Fig. 4b. The Al-HY zeolite exhibited no significant absorption bands. For the Zr-containing catalyst, two low-intensity bands at approximately 220 nm and 240 nm were observed, corresponding to dispersed ZrOx species and small ZrO_2 nanoclusters, respectively [65]. Nb-containing catalysts displayed strong absorption up to 350 nm. The monometallic Nb catalyst exhibited a maximum at ~ 280 nm, while the bimetallic Zr/Nb catalyst showed a slight red shift to ~ 290 nm, suggesting similar NbOx species in both catalysts [66]. The absence of a broad band beyond 400 nm indicates that bulk Nb_2O_5 did not form, even at high Nb loadings [67].

FTIR spectra of the catalysts are presented in Fig. 4c. The Al-HY support displayed characteristic bands of Y-zeolite [68], including a broad band between 800–1300 cm^{-1} associated with Si–O–Si and Al–O–Si asymmetric stretching, and bands between 570–710 cm^{-1} attributed to symmetric stretching of internal tetrahedra [69]. For Zr/Al-HY, these zeolite bands were retained, along with a peak at ~ 750 cm^{-1} assigned to Zr–O stretching vibrations [70]. In (Nb)Al-HY, the intensity of zeolite-related bands decreased, likely due to surface coverage by Nb species, and a band at ~ 675 cm^{-1} appeared, corresponding to Nb–O–Nb vibrations. The band at 850 cm^{-1}, characteristic of Nb=O stretching, was absent [71]. In the bimetallic 10Zr/(Nb)Al-HY catalyst, zeolite-related bands were further attenuated, while the

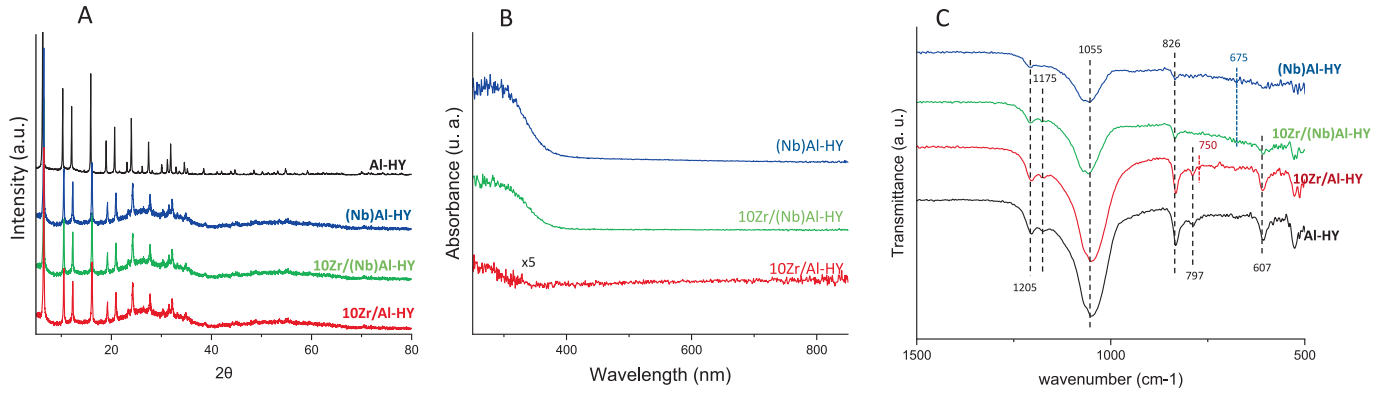

Fig. 4. XRD patterns (a), DR-UV–visible spectra (b) and FTIR spectra (c) of the catalysts and the support.

Nb–O–Nb band at 675 cm^{-1} was faintly visible, and no distinct Zr–O band was detected [72].

X-ray photoelectron spectroscopy (XPS) was performed to gain deeper insight into the surface composition and chemical environment of the catalysts. Fig. 5A shows the O 1 s spectral region, which can be deconvoluted into three components at 530.7–531.1 eV, 532.3–532.7 eV, and 533.2–533.6 eV. These peaks are assigned to oxygen in metal oxides (O–M), Si–O–Al, and Si–O–Si environments, respectively, with the dominant contributions arising from metal oxide and Si–O–Si domains.

Notably, the Zr/Al-HY catalyst exhibited higher binding energies for all three components (531.1, 532.7, and 533.6 eV), suggesting that Zr incorporation modifies the local environment of the zeolite framework. This effect is further supported by the relative contributions of each component compared to Nb-containing catalysts. For Zr/Al-HY, the Si–O–Si contribution accounted for approximately 70 at%, while the metal oxide contribution was only 18 at% (Table S4). In contrast, Nb-containing catalysts displayed a higher proportion of O–M species, consistent with their higher Nb loading (~40 wt%) compared to Zr (10 wt%).

Fig. 5B shows the Nb 3d spectral region, where the expected spin–orbit splitting between the $3d_{5/2}$ and $3d_{3/2}$ components (2.78 eV) was observed. The dominant contribution (~98 at%) corresponds to the Nb $3d_{5/2}$ peak at 207.4 eV, assigned to Nb^{5+} species, while a minor contribution at 205.6 eV is attributed to Nb^{4+} species [73,74]. The proportion of NbO_2 was 3.12 at% for (Nb)Al-HY and 1.94 at% for 10Zr/(Nb)Al-HY. A shift toward lower binding energies was detected in the bimetallic catalyst, indicating an increase in electron density around Nb atoms. This suggests a modified chemical environment, possibly due to interactions with Zr species, leading to a more reduced state or bonding with less electronegative elements [75].

Fig. 5C displays the Zr 3d spectral region, characterized by the Zr $3d_{5/2}$ peak at ~ 183 eV and a spin–orbit splitting of 2.4 eV, confirming the presence of Zr^{4+} species (as in ZrO_2) [76] in both catalysts. In the Nb-containing sample, a shift toward lower binding energy was observed, consistent with a different interaction between Zr and the Nb-modified zeolite compared to the pure zeolite. A lower binding energy means that the atom is more electron-rich, which could be related with a weaker Lewis acidity. This can be confirmed with the TPD-NH3 analysis of the sample, where the samples with Nb presented a weaker Lewis acidity [77]. Similar to the Nb 3d region, this shift suggests electronic modifications in the bimetallic catalyst, which may contribute to its enhanced catalytic performance.

Fig. 6 presents HR-TEM images of the supported Zr and/or Nb catalysts. Fig. 5A–B show representative images of the Zr/Al-HY catalyst. Zr species were observed in two distinct forms: (i) as porous ZrO_2 particles not interacting with the zeolitic support (Fig. 5A) and (ii) as highly dispersed ZrOx species homogeneously covering the support surface (Fig. 5B), as confirmed by elemental mapping. Although some isolated ZrO_2 nanoparticles were detected, their presence is consistent with XRD results, which showed no crystalline ZrO_2 reflections despite the relatively high Zr loading.

Fig. 6C–D display images of the (Nb)Al-HY catalyst. Niobium was well dispersed across the support, covering a significant portion of the zeolite surface. Based on previous studies [78] and the theoretical monolayer coverage of 5.8 Nb atoms nm^{-2} [55,56], the Nb loading

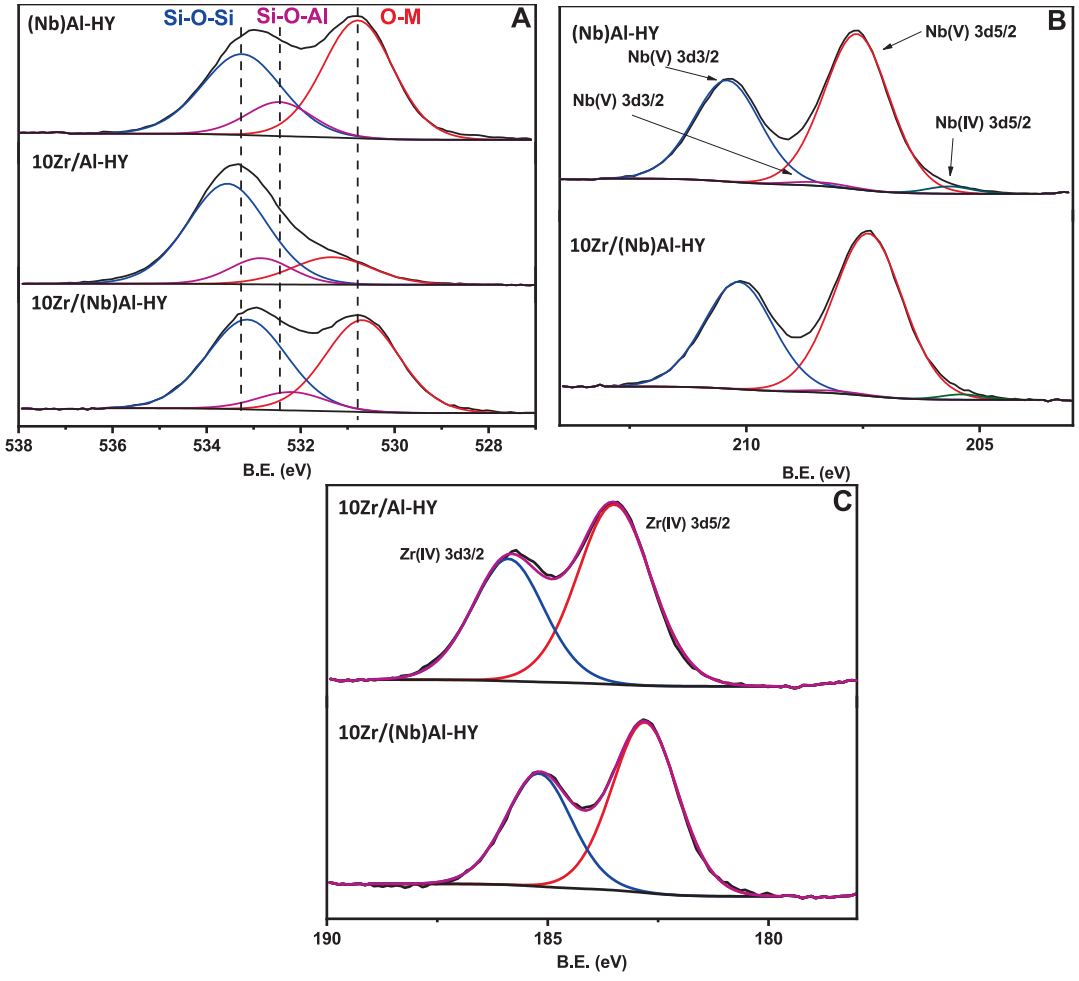

Fig. 5. XPS study of the catalysts synthesized based on Nb and Zr.

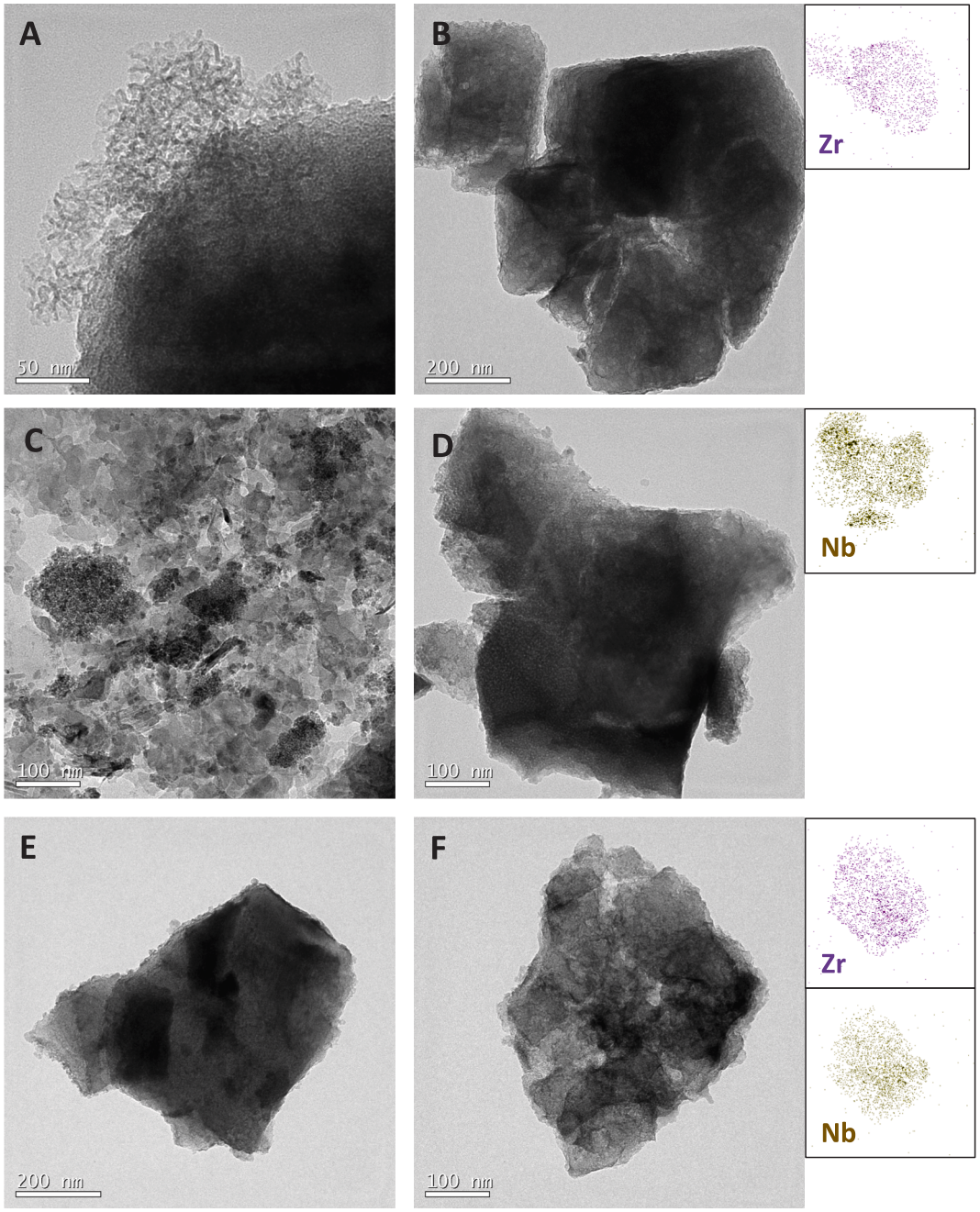

Fig. 6. TEM images of the catalysts Zr/Al-HY (A, B), (Nb)Al-HY (C, D) and 10Zr/(Nb)Al-HY (E, F).

should be sufficient to form a complete monolayer. The images confirm that NbOx species are primarily dispersed on the zeolite surface, although some Nb_2O_5 agglomerates (Fig. 6C) and Nb-free zones were also observed. The absence of Nb_2O_5 diffraction peaks in XRD corroborates the good dispersion of Nb species.

Fig. 6E–F show the 10Zr/(Nb)Al-HY bimetallic catalyst. This material was designed to deposit Zr species onto a NbOx monolayer covering the zeolite. While HR-TEM cannot resolve the exact depth distribution of Zr and Nb, the mapping indicates that both metals are co-located in the same regions, uniformly covering the zeolite surface. No areas containing only Zr or only Nb were detected, confirming strong Zr–Nb interaction, in agreement with XPS and UV–Vis results.

3.2. Catalytic results

Most studies on the transformation of furfural into GVL have been conducted in batch mode, while reports on continuous-flow processes are scarce. Therefore, we first evaluated the catalytic performance of the synthesized catalysts in batch to assess their activity for the target reaction. Based on these results, we then examined the stability and productivity of the catalysts. Operating under flow conditions offers several advantages, including shorter reaction times, rapid reagent mixing, improved heat transfer, simplified downstream processing, easier scale-up, and higher reactor volume productivity [79].

Batch reactions.

The catalysts were tested for the liquid-phase transformation of FF into GVL in batch mode at a standard reaction temperature of 180 °C (Table 3). For comparison, preliminary tests were carried out using bare

Table 3
Furfural transformation on Nb- and/or Zr- catalysts either bulk or supported on Al-HY zeolite in batch.[a]

Catalyst	FF conversion (%)	Yield to GVL (%)	Yield to IPL (%)	Yield to FAL (%)	Yield to FE (%)	Yield to other (%)	GVL Selectivity (%)
Al-HY	>99	0	79.9	0	0	20.1	0
Nb_2O_5	61.0	6.3	1.1	14.7	28.4	10.5	10.3
(Nb)Al-HY	>99	51.7	32.1	0	0	16.3	51.7
10Zr/(Nb)Al-HY	>99	67.0	20.7	0	0	12.4	67.0
Zr/Al-HY	>99	43.5	43.2	0	0	13.2	43.5
ZrO_2	>99	6.4	0	89.2	0	4.4	6.4

[a] Reaction conditions detailed in text (180 ºC and reaction time of 3 h).

zeolite, pure Nb_2O_5, and pure ZrO_2. When the bare support Al-HY was used, FF conversion was nearly complete (99.5 %); however, no traces of GVL were detected. In contrast, pure unsupported Nb_2O_5 achieved an FF conversion of approximately 60 %, but the GVL yield remained very low (around 4 %). The main products in this case were furfuryl ether (FE) and furfuryl alcohol (FAL). These results are pretty similar to thosee obtained in a previous study [80], where a higher proportion of Lewis acid sites compared to Bronsted ones implied the etherification of FAL to obtain FE takes place on Lewis acid sites. Finally, pure ZrO_2 was also tested, resulting in full FF conversion but only a modest GVL yield (6 %). Notably, a significant yield of FAL (almost 90 %) was obtained in this case. This result was compared with a previous study done [51,80,81], where Zr species produce a really high yield to FAL with a high selectivity.

For the Zr- and/or Nb-containing catalysts supported on zeolite, GVL formation increased significantly, which could be explained by the incorporation of both types of acid sites (Bronsted and Lewis) in the catalyst. Using Zr/Al-HY, complete FF conversion was achieved with a high GVL yield of 43.5 %. The catalyst containing niobium, (Nb)Al-HY, further improved the performance, reaching a GVL yield of 51.7 %. Interestingly, in both cases, a similarly high yield of isopropyl levulinate (IPL) was observed, while no formation of FE or FAL was detected.

Experiments with the Zr-based catalyst modified by the addition of a NbOx monolayer on the zeolite support, (10Zr/(Nb)Al-HY), resulted in complete FF conversion and the highest GVL yield (67 %). This corresponds to a 30–60 % increase compared to the monometallic catalysts. The enhanced GVL production occurred at the expense of IPL formation. In the previous sections, we focused on GVL formation. However, several intermediate products were also identified by GC–MS, including angelica lactone (AnL), levulinic acid (LA), furfuryl ether (FE), furfuryl alcohol (FAL), and isopropyl levulinate (IPL). Additionally, by-products similar to those reported in earlier studies [37,54] were detected, such as 3-penten-1-ol, 2-cyclopenten-1-one, 1,4-pentanediol, and 2-pentenoic acid.

To confirm that the exceptional performance was not solely due to the total metal content but rather to the coexistence of Zr and Nb, monometallic catalysts containing the same total amounts of Zr or Nb as the optimal catalyst (10Zr/(Nb)Al-HY) were synthesized and tested. These catalysts, designated as Nb2/Al-HY (containing only Nb) and Zr2/Al-HY (containing only Zr), were evaluated under identical reaction conditions (Table S5). In both cases, GVL yields remained below 50 %, and the formation of other by-products was considerably higher compared to the bimetallic catalyst.

Reactions at different times were carried out with the optimal catalyst (10Zr/(Nb)Al-HY) to gain deeper insight into the possible reaction network. Fig. 7 shows the evolution of product yields as a function of reaction time. After 1 h, FF was completely converted, yielding a moderate amount of GVL (32 %) along with significant quantities of IPL, FE, and other products. After 3 h, the GVL yield increased substantially to 67 %, while the formation of other products decreased to below 13 %. During this interval (1–3 h), the IPL yield slightly decreased, and all FE was converted into IPL and GVL. After 5 h, the IPL yield continued to decline slightly in favor of GVL, which showed only a marginal increase. The yield of other products remained nearly constant. These results confirm, as reported in previous studies [16], that the conversion of IPL

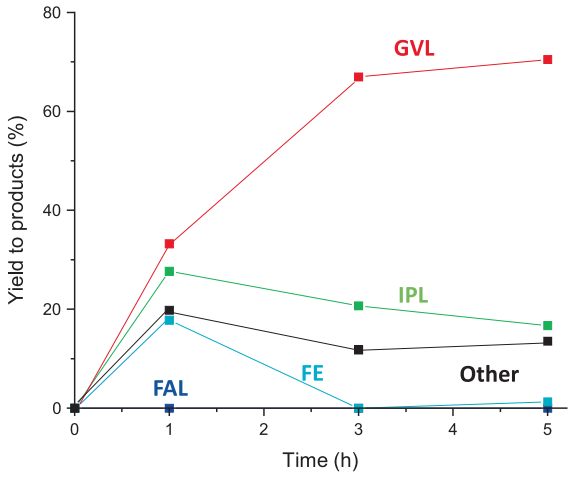

Fig. 7. Evolution of the yields to the representative reaction products during the furfural transformation on 10Zr/(Nb)Al-HY catalyst with the reaction time. Reaction conditions: 5 mL of 2-propanol, 0.125 mmol of FF, 0.1 g of catalyst, 180 °C, batch.

into GVL is the rate-determining step and requires extended reaction times to maximize GVL yield and minimize IPL. However, no significant improvement in GVL yield was observed beyond 3 h, suggesting a plateau likely caused by GVL reaching its maximum concentration, after which decomposition into undesired by-products may occur. In any case, the yields of other products only moderately increase after 3 h.

The recyclability of the 10Zr/(Nb)Al-HY catalyst under batch conditions was also evaluated (Fig. 8A) under typical reaction conditions (0.1 g of catalyst and 25 mM FF in 2-propanol at 180 °C) for 1 h over five consecutive cycles. The catalyst exhibited high catalytic activity in the first run (32 % GVL yield), with a slight increase in the second cycle (36 %). From the third to the fifth cycle, a minor decrease in GVL yield was observed (27–30 %). Although these variations are not substantial, the slight decline in the fifth cycle compared to the first may be attributed to partial deactivation of active sites or possible leaching of active metals.

XRD analysis of the catalyst after three cycles (Fig. S2) revealed the formation of Nb_2O_5; however, this phase does not appear to significantly affect catalytic activity. To determine whether leaching contributed to deactivation, an additional test was performed (Fig. 8B). After a standard 1 h reaction, the catalyst was removed by filtration, and the liquid phase was subjected to an additional 2 h reaction under identical conditions. No further conversion was observed, suggesting the absence of leaching. This conclusion was further supported by ICP analysis, which showed no significant difference in Zr and Nb content between the fresh catalyst and the sample used for three cycles.

As reported in previous studies [32,37,46,54,82], the transformation of FF into GVL proceeds through a cascade reaction involving several intermediates (Fig. 9). This network includes steps governed by the Meerwein–Ponndorf–Verley (MPV) mechanism as well as reactions catalyzed by Lewis acid sites (LAS) and/or Brønsted acid sites (BAS).

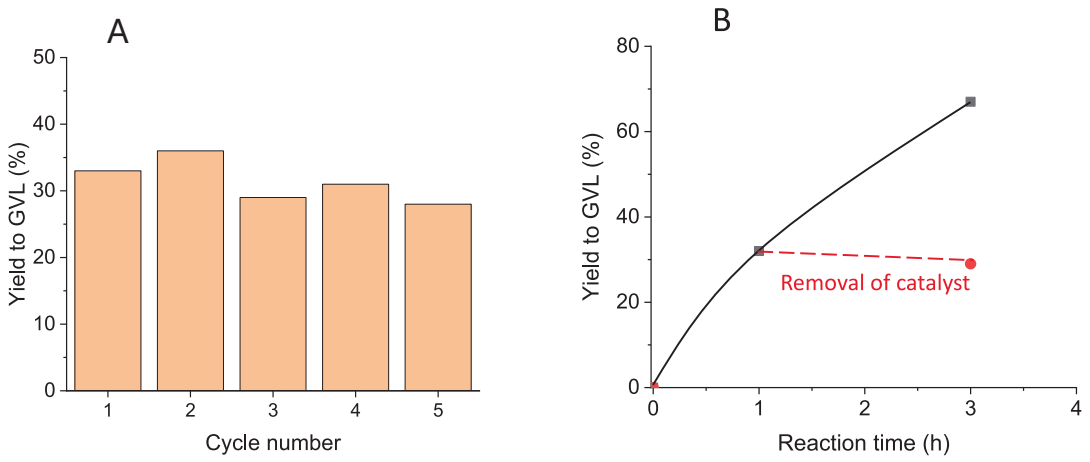

Fig. 8. A) Recycling test of the catalyst 10Zr/(Nb)Al-HY. Reaction conditions: 5 mL of 2-propanol, 0.125 mmol of FF, 0.1 g of catalyst, 180 °C for 1 h. B) Evolution of the yield to GVL with the reaction time either maintaining the catalysts in the reaction mixture (■) or removing the catalyst after 1 h (●).

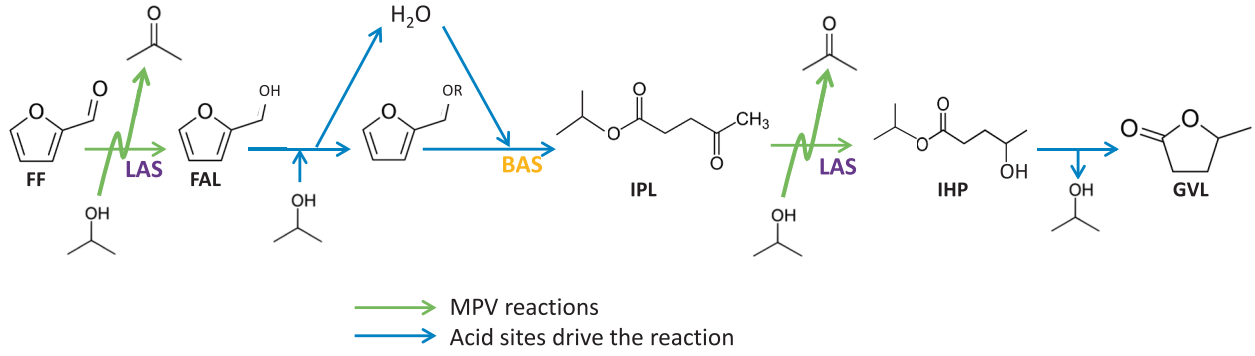

Fig. 9. Reaction mechanism to transform FF in GVL in one-pot according to the catalytic results obtained and previous studies.

Initially, FF is reduced to FAL via the MPV reaction, facilitated by LAS provided by metal oxide centers. Subsequently, FAL undergoes esterification to form FE, releasing a water molecule; this step requires both BAS and LAS. FE can then react with water through a ring-opening reaction to produce IPL, a process promoted by BAS. IPL is further hydrogenated to isopropyl 4-hydroxypentanoate (IHP) via the MPV mechanism, and finally, IHP cyclizes to GVL in the presence of both BAS and LAS.

As proposed in earlier studies [51], the zeolite provides Brønsted acid sites (with a BAS/LAS ratio of approximately 2), while the metal oxide centers supply Lewis acid sites. Incorporating metal oxides into the support decreases the BAS/LAS ratio, and this effect becomes more pronounced at higher metal loadings. Therefore, controlling and tuning the BAS/LAS ratio is essential for optimizing catalytic performance. In this case and due to the high yields to IPL, the step to convert IPL into GVL could be the rate-determining step. Thus, if higher yields to GVL are desired, longer reaction times would be required.

The superior catalytic activity of the bimetallic catalyst compared to the monometallic counterparts can be attributed to several factors. One key factor is its intermediate acidity, which is neither too high—avoiding polymerization and humin formation—nor too low, which would slow down the intermediate steps in the FF-to-GVL transformation, as reported in previous studies [37,40,83]. The bimetallic catalyst exhibited an intermediate acid density per surface area (higher than 10Zr/Al-HY but lower than (Nb)Al-HY).

Another important feature is the homogeneous dispersion of nanoparticles in the bimetallic system. This high dispersion provides a greater number of accessible active sites, enabling more efficient catalytic performance. Additionally, the presence of two types of active sites (Zr and Nb) likely contributes to the enhanced activity compared to monometallic catalysts. Previous studies [53,84,85] have shown that nanoparticle dispersion is a critical factor for catalytic efficiency, and this effect was more pronounced in the bimetallic catalyst, whereas some aggregation of Zr- or Nb-oxide was observed in the monometallic samples (Fig. 6).

Furthermore, XPS analysis revealed differences in the electronic environment of surface Zr and Nb between mono- and bimetallic catalysts. Specifically, shifts to lower binding energies for Zr $3d_{3/2}$, Zr $3d_{5/2}$, Nb $3d_{3/2}$, and Nb $3d_{5/2}$ were observed in the bimetallic catalyst, which may correlate with its higher catalytic activity.

Overall, the bimetallic catalyst combines optimal acidity, superior nanoparticle dispersion, and synergistic electronic effects, resulting in the most favorable characteristics for high catalytic activity and selectivity toward GVL from FF.

Catalytic tests in continuous regime.

The transformation of FF into GVL has been extensively studied under batch conditions; however, its application in continuous-flow systems has been scarcely explored, and the reported results remain relatively modest [52,53]. Given the notable performance of the synthesized Zr/Nb catalysts in batch reactors, their behavior under continuous-flow conditions was evaluated. For this purpose, a custom-designed liquid-phase fixed-bed reactor was employed. These experiments aimed to determine whether the bimetallic catalyst could outperform the monometallic catalysts, as observed in batch tests.

Preliminary experiments were conducted using (Nb)Al-HY to establish optimal operating conditions. This catalyst was selected because its performance in batch mode was intermediate among the three catalysts under study. The temperature and FF concentration were maintained at

the same values as in batch reactions (180 °C and 25 mM, respectively), while the contact time was optimized. Two initial tests were performed with contact times of 10 min—previously reported as optimal [52,53]—and 5 min. The results of these tests are shown in Figs. S3 and S4, with a comparison presented in Fig. 10. Longer contact times favored higher selectivity toward GVL but also increased the proportion of undesired by-products ("others"), while reducing intermediate concentrations. Since the objective of this work is to maximize GVL selectivity while minimizing by-product formation, a contact time of 5 min was selected for catalyst screening. This choice also preserves the presence of intermediates, providing valuable insights into the catalytic behavior of the different materials. Further studies were then carried out to investigate the influence of contact time on the best-performing catalyst.

After selecting the optimal contact time, additional tests were performed by adding an equivalent amount of water to assess its influence and eliminate any potential effect from the water generated or consumed during the reaction. As illustrated in Fig. 9, water participates in multiple steps of the cascade reaction converting FF to GVL: it is produced during FE formation, required for IPL generation, and involved in the equilibrium between FAL and AnL. Fig. 11 presents the average results after 24 h of continuous-flow operation. The selectivity (and yield) to AnL, levulinic acid, and GVL remained nearly unchanged regardless of water addition. However, the presence of added water increased the selectivity toward IPL while suppressing the formation of other undesired by-products.

The influence of water on this reaction has been investigated by our group in batch mode [60]. The results showed that product selectivity is affected by the amount of water present in the reaction system, largely due to the formation of diisopropyl ether via etherification of two isopropanol molecules. This step generates water and it is itself sensitive to reaction temperature, as the degree of solvent dehydration varies. In addition, an improved carbon balance (i.e., a lower proportion of "Others") was observed. This was attributed to the suppression of the main pathway responsible for carbon losses, namely, the formation of humins from FAL. This process begins with the etherification of two FAL molecules to form difurfuryl ether (DFE), an equilibrium reaction that releases water. Consequently, adding water to the system inhibits this step and thus mitigates humins formation.

XRD patterns of the fresh Nb/Al-HY catalyst as well as those used with or without water in the feed are shown in Fig. S5. Conversely to the fresh catalyst, peaks related to Nb_2O_5 crystalline phase are present for both used catalysts.

Once the optimal contact time ($\tau = 5$ min) was established and the influence of water evaluated, reactions were performed using both

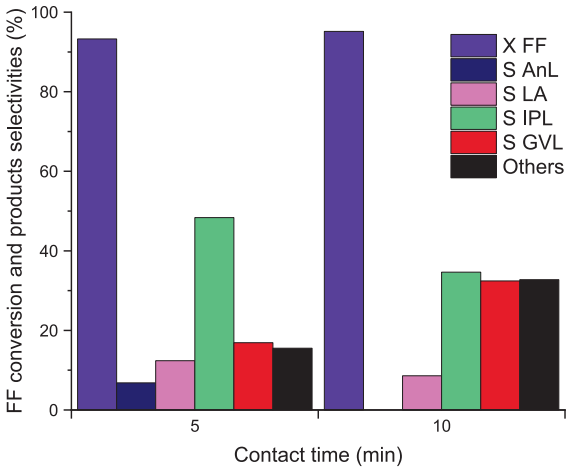

Fig. 10. Comparison of furfural conversion and products selectivities (%) using (Nb)Al-HY with different contact time; working conditions: 180 °C, [FF] = 25 mM.

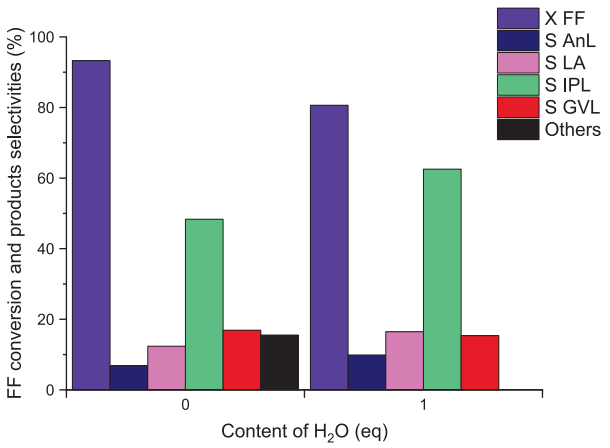

Fig. 11. Influence of the content of H_2O on furfural conversion and products selectivities (%) using (Nb)Al-HY.

monometallic and bimetallic catalysts. Fig. 12a compares the average results obtained with the different catalysts over 8 h of continuous operation. When using Zr/Al-HY, complete FF conversion was achieved. The main product was IPL, with a selectivity of approximately 50 %, while GVL selectivity reached 20 %. Additionally, the formation of undesired by-products ("Others") exceeded 20 %.

In contrast, the bimetallic catalyst 10Zr/(Nb)Al-HY delivered the highest GVL selectivity (40 %), along with complete FF conversion and 30 % selectivity toward IPL. However, this catalyst also exhibited appreciable formation of undesired by-products. On the other hand, (Nb)Al-HY resulted in partial FF conversion, with IPL as the predominant product (60 % selectivity) and GVL selectivity below 20 %. Notably, no undesired by-products were detected in this case.

These results suggest a clear synergistic effect between Zr and Nb, enhancing GVL formation under continuous-flow conditions compared to the monometallic catalysts. Nb, which could favour certain steps in the one-pot transformation of FF into GVL. However, IPL conversion appears to be somewhat limited when using the bimetallic catalyst. This limitation may be attributed to an insufficient density and/or strength of Lewis acid sites to promote the conversion of levulinate to the final product. Indeed, the highest GVL selectivity was observed with the catalyst exhibiting the greatest Lewis acidity among those studied (Fig. 13a). Conversely, the correlation between GVL selectivity and Brønsted acidity indicates that the bimetallic catalyst possesses an optimal acidity level, as deviations in either direction (increase or decrease) result in poorer performance (Fig. 13b). A similar trend was observed for GVL selectivity as a function of the BAS/LAS ratio (Fig. 13c). As previously reported in the literature, these correlations confirm that, for this reaction, it is not the total acidity but rather the BAS/LAS ratio that plays a critical role.

Since the bimetallic catalyst 10Zr/(Nb)Al-HY exhibited the best performance, it was selected for further studies to better understand the reaction mechanism and reduce the formation of undesired products ("Others") (Fig. 14). Four tests were conducted at different contact times (1.25, 2.5, 5, and 10 min), each lasting 48 h. In all cases, FF conversion was very high (93–100 %), increasing as expected with contact time (Fig. 14). Regarding product selectivity, distinct trends were observed. GVL selectivity increased with contact time, reaching a maximum of approximately 40 %, similar to the value obtained after 1 h in batch conditions. Conversely, selectivity toward intermediates such as AnL and LA decreased markedly, and at contact times of 5 min or longer, only trace amounts of these compounds were detected. IPL selectivity remained relatively constant at around 35–40 % across all conditions. These results suggest that AnL is the intermediate most readily converted into GVL, whereas IPL conversion appears to be hindered, as previously hypothesized. Moreover, the formation of unidentified

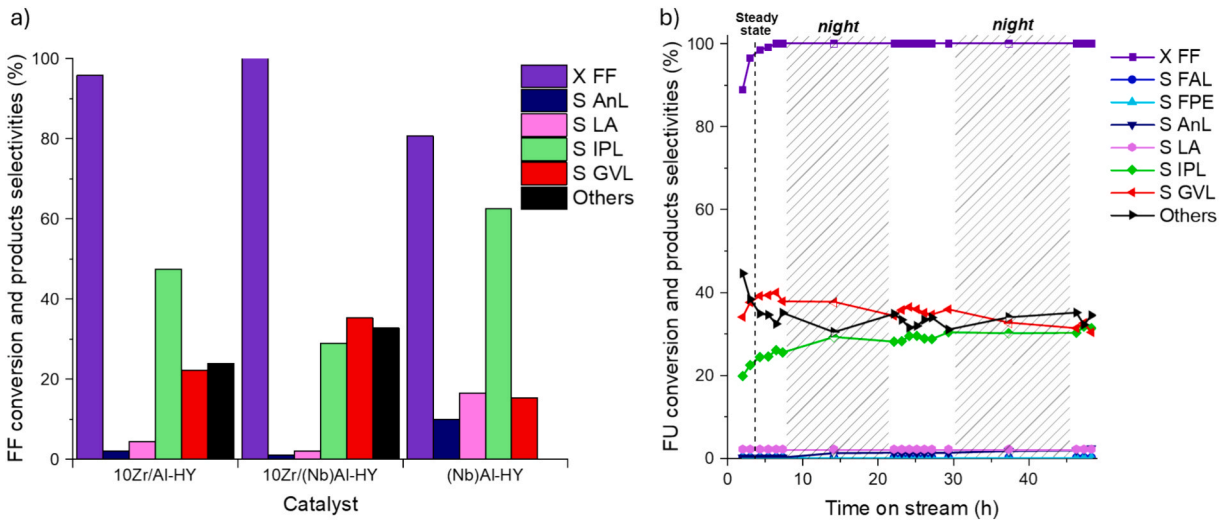

Fig. 12. (a) Furfural conversion and products selectivities (%) comparison using (Nb)Al-HY, 10Zr/Al-HY or 10Zr/(Nb)Al-HY; (b) FF conversion and products selectivity (%) over the time on stream (h) on 10Zr(Nb)/Al-HY; Reaction conditions: 180 °C, [FF] = 25 mM, τ = 5 min, 1 eq H_2O.

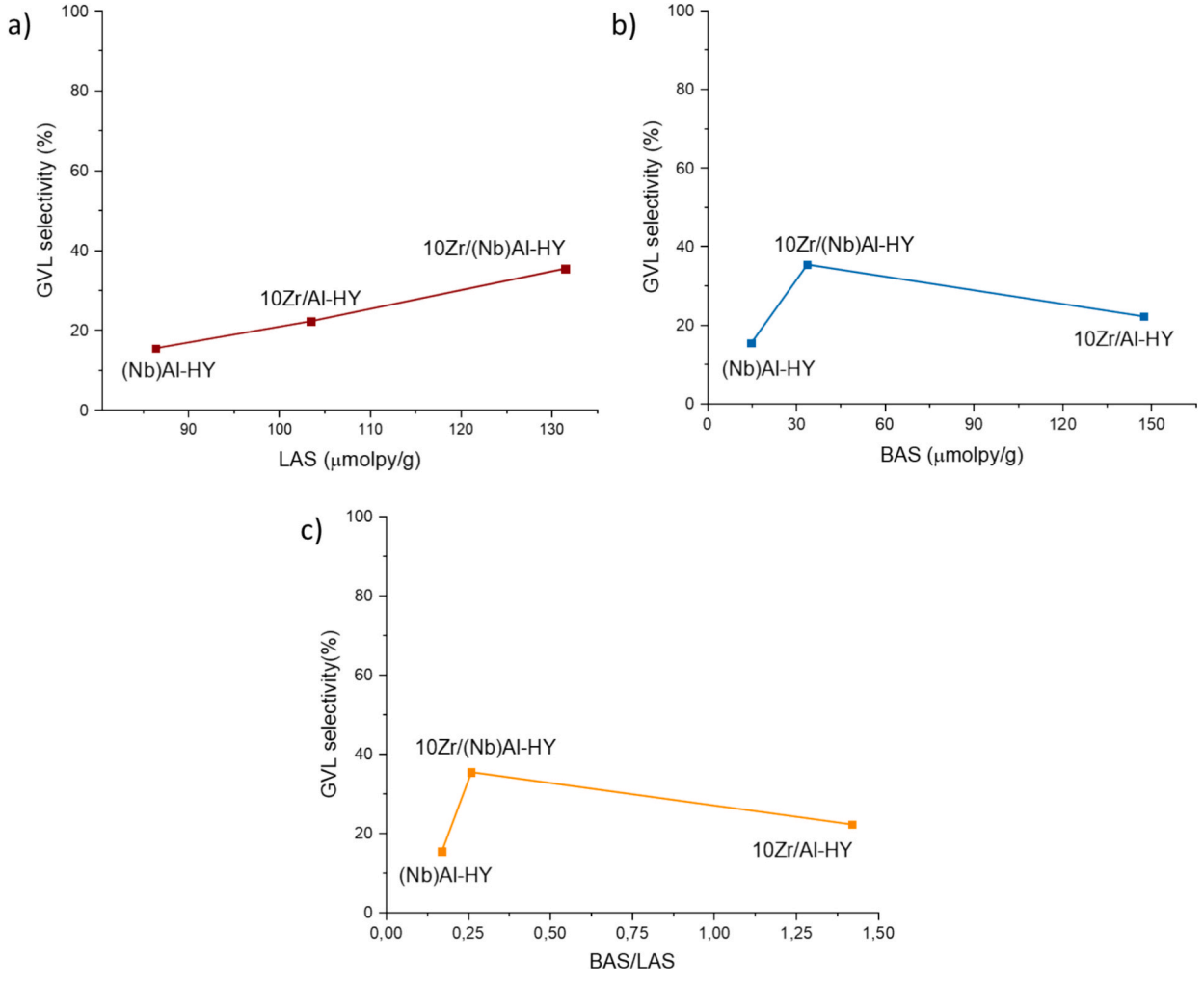

Fig. 13. GVL selectivity respect to a) LAS (μmolpy/g), b) BAS (μmolpy/g) and c) BAS/LAS ratio.

products ("Others") did not follow a linear trend.

The fresh and used 10Zr/(Nb)Al-HY catalysts (T = 180 °C, [FF] = 25 mM, 1 eq H_2O, τ = 5 min) were characterized by XRD, NH_3-TPD, and TGA to assess possible structural changes after reaction.

XRD analysis was performed before and after use to detect any morphological differences. As shown in Fig. 15A, characteristic diffraction peaks of Nb_2O_5 appeared in the used catalyst but were absent in the fresh sample. These findings are consistent with observations from

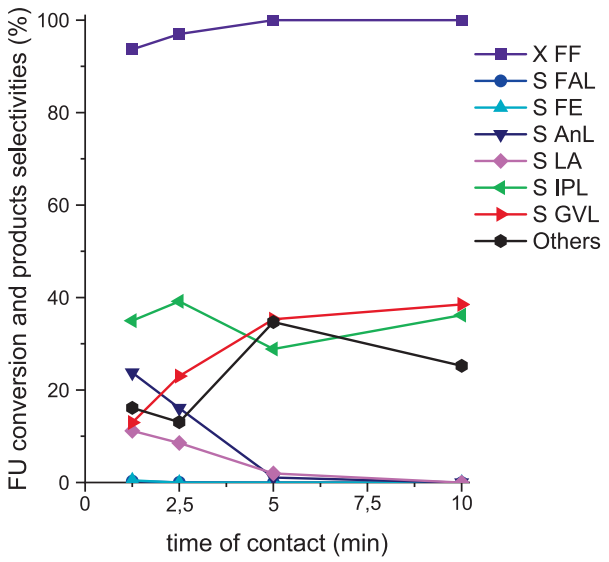

Fig. 14. Influence of the contact time over the furfural conversion and the selectivity to the main reaction products using 10Zr/(Nb)Al-HY catalyst. Working conditions: 180 °C, [FF] = 25 mM, 1 eq H_2O.

the batch reaction (Fig. S2) and suggest that Nb may undergo structural changes under reaction conditions. However, this instability does not appear to affect the active phase, as the catalyst remained stable for over 30 h on stream (Fig. 12b), where FF conversion and selectivity to the main products remained constant. Only after approximately 30 h was a slight decrease in GVL selectivity observed, accompanied by an increase in undesired products. No diffraction peaks corresponding to ZrO_2 were detected in any sample.

NH_3-TPD analysis of the bimetallic catalyst revealed a decrease in acid site density after use (Fig. 15B), likely due to partial coverage by carbonaceous deposits. However, the maximum NH_3 desorption temperature remained unchanged compared to the fresh catalyst, indicating that the strength of the acidic sites was preserved, which may explain the observed catalytic stability. Thermogravimetric analysis (TGA) was performed on the fresh and used bimetallic catalysts to investigate whether the unidentified products could be correlated with weight loss (Fig. 15C). Two distinct weight-loss events were observed: the first, around 100 °C, corresponds to water desorption; the second can be attributed to heavy organic molecules formed from furfural degradation (humins). Comparing the fresh and used catalysts, only a 3.52 % weight loss was associated with these heavy organic deposits, which does not account for the entire carbon loss observed.

Overall, the bimetallic Zr–Nb catalyst supported on Y-zeolite demonstrated high efficiency for the transformation of furfural into γ-valerolactone under both batch and continuous-flow conditions, even though some structural rearrangement occurred during the reaction. Notably, the results obtained in continuous flow represent the best

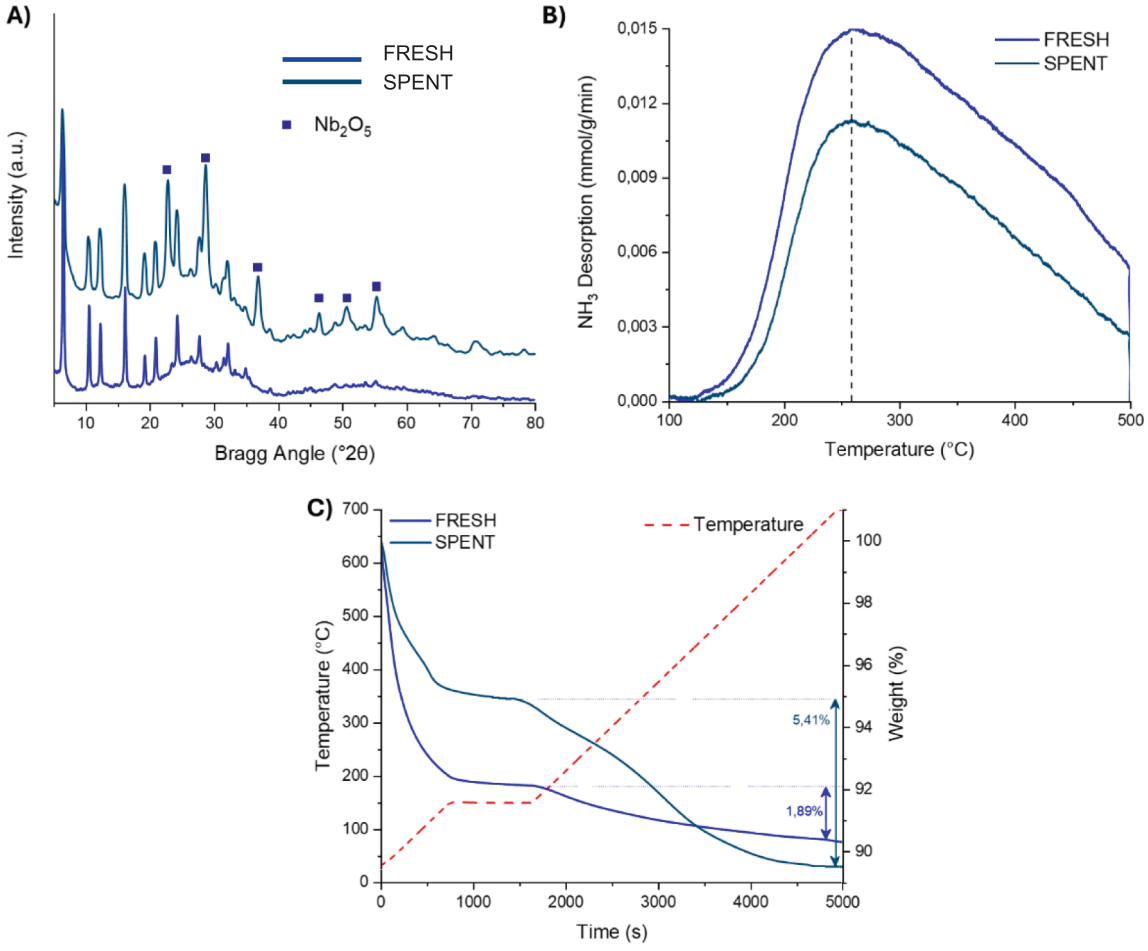

Fig. 15. Comparison between fresh and used 10Zr/(Nb)Al-HY catalyst in continuous reaction by different techniques: XRD (A), NH_3-TPD analysis (B) and TGA (C).

reported to date, achieving GVL yields of approximately 40 % and a space–time yield (STY) of 1,103 μmol GVL · g_{cat}^{-1} · h^{-1} (Fig. 16 and Table S6). The catalyst exhibited stable behavior over time on stream, with only a slight decline in performance after 48 h. This moderate decrease in GVL formation could be attributed to: (i) sintering of NbOx species into crystalline Nb_2O_5, leading to a slight reduction in Nb active sites, and (ii) the formation of carbonaceous deposits on the catalyst surface, partially blocking active sites.

Furthermore, the continuous-flow results are comparable to those obtained in batch after 1 h of reaction, considering that FF conversion in batch exceeds 99 %, allowing direct comparison of yields with selectivity values in continuous mode.

4. Conclusions

γ-Valerolactone (GVL) is a highly valuable chemical that can be produced from furfural in a one-step process using catalysts based on Zr and Nb supported on commercial Y-zeolite. While pure metal oxides such as ZrO_2 and Nb_2O_5 can catalyze this transformation, the resulting GVL yields are very low. Supporting these metals on Y-zeolite significantly improves performance, as the zeolite provides Brønsted acid sites and the metal oxides supply Lewis acid sites—both essential for the cascade reaction steps.

The bimetallic Zr–Nb catalyst exhibited superior performance compared to the monometallic counterparts, achieving higher GVL selectivity in both batch (67 %) and continuous-flow conditions (40 %). This improvement is attributed not only to the increased number of active sites but also to a synergistic effect between Zr and Nb, which enhances GVL yields at longer reaction times while minimizing undesired by-products. The higher dispersion of metallic species in the bimetallic catalyst likely contributes to its enhanced activity.

In batch mode, the Zr-based catalyst maintained high GVL yields, while in the bimetallic system, Nb further promoted GVL formation. Additionally, the bimetallic catalyst demonstrated good stability after several uses in batch and after 48 h of continuous operation. Characterization data revealed structural rearrangements during reaction, yet the catalyst remained active and relatively stable, delivering high GVL yields.

Importantly, the continuous-flow results represent a significant improvement over previous studies, where high yields of intermediates and undesired products were typically observed. These findings highlight the potential of Zr–Nb/Y-zeolite catalysts for efficient, scalable production of GVL from furfural.

Declaration of generative AI and AI-assisted technologies in the manuscript preparation process

During the preparation of this work the authors made occasional use of Chat GPT in order to refine the wording of specific sentences in English. After using this tool/service, the authors reviewed and edited the content as needed and take full responsibility for the content of the published article.

CRediT authorship contribution statement

Adrián García: Writing – original draft, Investigation. **Anna Saotta:** Writing – original draft, Investigation. **Elianny Da Silva:** Resources, Investigation. **Pablo J. Miguel:** Validation, Formal analysis. **Alessandro Allegri:** Project administration, Data curation. **Rita Sánchez-Tovar:** Investigation, Funding acquisition. **Jean-Charles Morin:** Investigation. **Olivier Gardoll:** Investigation. **Tomás García:** Resources, Investigation. **José Manuel López:** Resources, Investigation. **Stefania Albonetti:** Validation, Funding acquisition, Conceptualization. **Nikolaos Dimitratos:** Supervision, Conceptualization. **Benjamin Solsona:** Writing – review & editing, Supervision, Funding acquisition, Conceptualization.

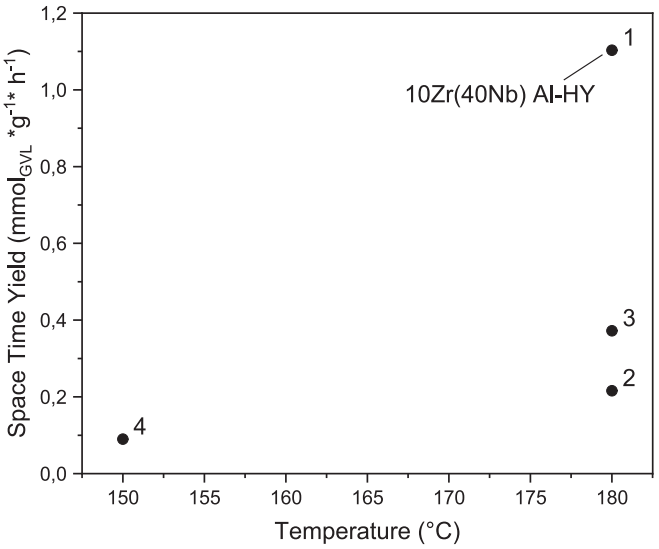

Fig. 16. Comparison of the GVL Space Time Yields (μmol$_{GVL}$* g^{-1} *h^{-1}) achieved on furfural by the prepared catalyst in comparison to the results published in literature for the same reaction. The labels refer to the entries in Table S6.

Declaration of competing interest

The authors declare that they have no known competing financial interests or personal relationships that could have appeared to influence the work reported in this paper.

Acknowledgements

The authors would like to acknowledge the Generalitat Valenciana for CIAICO/2024/087 and CIGRIS/2022/198. The authors also thank the Ministerio de Ciencia e Innovación-Agencia Estatal de Investigación and European Union NextGeneration EU through the projects PID2021–126235OB-C33 MCIN/AEI/10.13039/ 501100011033/ FEDER Una manera de hacer Europa, UE and TED2021–129555B–I00/ AEI/10.13039/501100011033/Unión Europea NextGenerationEU/ PRTR.

Appendix A. Supplementary data

Supplementary data to this article can be found online at https://doi.org/10.1016/j.fuel.2025.138062.

Data availability

Data will be made available on request.

References

[1] Oubraham A, Zaccour G. A survey of applications of viability theory to the sustainable exploitation of renewable resources. Ecol Econ 2018;145:346–67. https://doi.org/10.1016/j.ecolecon.2017.11.008.
[2] Yusuf AM, Abubakar AB, Mamman SO. Relationship between greenhouse gas emission, energy consumption, and economic growth: evidence from some selected oil-producing african countries. Environ Sci Pollut Res 2020;27:15815–23. https://doi.org/10.1007/s11356-020-08065-z.
[3] Wu D, Liu S, Nie Y, Sun D, Zhou Y, Yang S, et al. Electrocatalytic upgrading of glycerol into high-value products: Catalyst design, process engineering, and economic assessment. Chem Eng J 2025;518:164511. https://doi.org/10.1016/j.cej.2025.164511.
[4] Stančin H, Mikulčić H, Wang X, Duić N. A review on alternative fuels in future energy system. Renew Sustain Energy Rev 2020;128:109927. https://doi.org/10.1016/j.rser.2020.109927.
[5] Holechek JL, Geli HME, Sawalhah MN, Valdez R. A global assessment: can renewable energy replace fossil fuels by 2050? Sustainability 2022;14:4792. https://doi.org/10.3390/su14084792.

[6] Yan Q, Zhou Y, Zhang Y, Sun D, Wu X, Yang S, et al. Rational Design of Advanced Functional Catalysts for Photo-Reforming Glucose into Bio-Derived Fuels and Chemicals. Adv Sci 2025;12:e08850. https://doi.org/10.1002/advs.202508850.

[7] Tian H, Wang A, Pan H, Zhang H, Yang S. Advances and perspectives on photochemical/electrochemical synthesis of nitrogen, sulfur, and phosphorus heteroatom containing compounds from biomass-based feedstocks. Ind Crop Prod 2024;222:119738. https://doi.org/10.1016/j.indcrop.2024.119738.

[8] Román-Leshkov Y, Barrett CJ, Liu ZY, Dumesic JA. Production of dimethylfuran for liquid fuels from biomass-derived carbohydrates. Nature 2007;447:982–5. https://doi.org/10.1038/nature05923.

[9] Miyazawa T, Koso S, Kunimori K, Tomishige K. Development of a Ru/C catalyst for glycerol hydrogenolysis in combination with an ion-exchange resin. Appl Catal A 2007;318:244–51. https://doi.org/10.1016/j.apcata.2006.11.006.

[10] Barla MK, Velagala RR, Minpoor S, Madduluri VR, Srinivasu P. Biomass derived efficient conversion of levulinic acid for sustainable production of γ-valerolactone over cobalt based catalyst. J Hazard Mater 2021;405:123335. https://doi.org/10.1016/j.jhazmat.2020.123335.

[11] Perea-Moreno MA, Samerón-Manzano E, Perea-Moreno A-J. Biomass as renewable energy: worldwide research trends. Sustainability 2019;11:863. https://doi.org/10.3390/su11030863.

[12] Cherubini F. The biorefinery concept: using biomass instead of oil for producing energy and chemicals. Energy Conv Manag 2010;51:1412–21. https://doi.org/10.1016/j.enconman.2010.01.015.

[13] Galletti AMR, Antonetti C, Luise VD, Martinelli M. A sustainable process for the production of γ-valerolactone by hydrogenation of biomass-derived levulinic acid. Green Chem 2012;14:688–94. https://doi.org/10.1039/C2GC15872H.

[14] Yadav M, Goel G, Hatton FL, Bhagat M, Mehta SK, Mishra RK, et al. A review on biomass-derived materials and their applications as corrosion inhibitors, catalysts, food and drug delivery agents. Curr Res Green Sustain Chem 2021;4:100153. https://doi.org/10.1016/j.crgsc.2021.100153.

[15] Zhao H, Holladay JE, Brown H, Zhang ZC. Metal Chlorides in Ionic Liquid Solvents Convert Sugars to 5-Hydroxymethylfurfural. Science 2007;316:1597–600. https://doi.org/10.1126/science.1141199.

[16] García A, Miguel PJ, Ventimiglia A, Dimitratos N, Solsona B. Optimization of the Zr-loading on siliceous support catalysts leads to a suitable Lewis/Brønsted acid sites ratio to produce high yields to γ-valerolactone from furfural in one-pot. Fuel 2022;324:124549. https://doi.org/10.1016/j.fuel.2022.124549.

[17] Menegazzo F, Ghedini E, Signoretto M. 5-Hydroxymethylfurfural (HMF) production from Real Biomasses. Molecules 2018;23:2201. https://doi.org/10.3390/molecules23092201.

[18] Birgen C, Dürre P, Preisig HA, Wentzel A. Butanol production from lignocellulosic biomass: revisiting fermentation performance indicators with exploratory data analysis. Biotechnol Biofuels 2019;12:167. https://doi.org/10.1186/s13068-019-1508-6.

[19] Rajeswari S, Baskaran D, Saravanan P, Rajasimman M, Rajamohan N, Vasseghian Y. Production of ethanol from biomass – recent research, scientometric review and future perspectives. Fuel 2022;317:123448. https://doi.org/10.1016/j.fuel.2022.123448.

[20] Horváth IT, Mehdi H, Fábos V, Boda L, Mika TL. γ-Valerolactone—a sustainable liquid for energy and carbon-based chemicals. Green Chem 2008;10:238–42. https://doi.org/10.1039/B712863K.

[21] Wang H, Wu Y, Li Y, Peng J, Gu X-K, Ding M. One-step synthesis of gasoline fuels from γ-valerolactone with high selectivity over Cu/HZSM-5 bifunctional catalyst. Appl Catal B Environ 2021;296:120338. https://doi.org/10.1016/j.apcatb.2021.120338.

[22] García A, Sanchis R, Llopis FJ, Vázquez I, Pico MP, López ML, et al. Ni supported on natural clays as a catalyst for the transformation of levulinic acid into γ-valerolactone without the addition of molecular hydrogen. Energies 2020;13:3448. https://doi.org/10.3390/en13133448.

[23] Kerkel F, Markiewicz M, Stolte S, Müller E, Kunz W. The green platform molecule gamma-valerolactone – ecotoxicity, biodegradability, solvent properties, and potential applications. Green Chem 2021;23:2962–76. https://doi.org/10.1039/D0GC04353B.

[24] Zhang Z. Synthesis of γ-valerolactone from carbohydrates and its applications. ChemSusChem 2016;9:156–71. https://doi.org/10.1002/cssc.201501089.

[25] Dutta S, Yu IKM, Tsang DCW, Ng YH, Ok YS, Sherwood J, et al. Green synthesis of gamma-valerolactone (GVL) through hydrogenation of biomass-derived levulinic acid using non-noble metal catalysts: a critical review. Chem Eng J 2019;372:992–1006. https://doi.org/10.1016/j.cej.2019.04.199.

[26] García A, Miguel PJ, Pico MP, Álvarez-Serrano I, López ML, García T, et al. γ-valerolactone from levulinic acid and its esters: Substrate and reaction media determine the optimal catalyst. Appl Catal A 2021;623:118276. https://doi.org/10.1016/j.apcata.2021.118276.

[27] Peng Q, Wang H, Xia Y, Liu X. One-pot conversion of furfural to gamma-valerolactone in the presence of multifunctional zirconium alizarin red S hybrid. Appl Catal A 2021;621:118203. https://doi.org/10.1016/j.apcata.2021.118203.

[28] Zhang L, Xi G, Yu K, Yu H, Wang X. Furfural production from biomass–derived carbohydrates and lignocellulosic residues via heterogeneous acid catalysts. Ind Crop Prod 2017;98:68–75. https://doi.org/10.1016/j.indcrop.2017.01.014.

[29] Yong KJ, Wu TY, Lee CBTL, Lee ZJ, Liu Q, Jahim JM, et al. Furfural production from biomass residues: current technologies, challenges and future prospects. Biomass Bioenergy 2022;161:106458. https://doi.org/10.1016/j.biombioe.2022.106458.

[30] Molina MJC, Granados ML, Gervasini A, Carniti P. Exploitment of niobium oxide effective acidity for xylose dehydration to furfural. Catal Today 2015;254:90–8. https://doi.org/10.1016/j.cattod.2015.01.018.

[31] Zhao K, Wen B, Tang Q, Wang F, Liu X, Xu Q, et al. Recent catalytic innovations in furfural transformation. Green Chem 2024;26:9957–92. https://doi.org/10.1039/D4GC01983K.

[32] Melero JA, Morales G, Iglesias J, Paniagua M, López-Aguado C. Rational optimization of reaction conditions for the one-pot transformation of furfural to γ-valerolactone over Zr–Al-Beta Zeolite: Toward the efficient utilization of biomass. Ind Eng Chem Res 2018;57:11592–9. https://doi.org/10.1021/acs.iecr.8b02475.

[33] Mutlu B, Unal B, Unlu D. A novel and clean technique for the one-pot production of green chemical γ-valerolactone from furfural using bifunctional H3PW12O4/UiO-66 catalyst: Pervaporation membrane reactor. J Environ Chem Eng 2024;12:112665. https://doi.org/10.1016/j.jece.2024.112665.

[34] Ma M, Hou P, Zhang P, Guo Q, Yue H, Huang J, et al. Tandem catalysis of furfural to γ-valerolactone over polyoxometalate-based metal-organic frameworks: Exploring the role of confinement in the catalytic process. Renew. Energy 2024;227:120474. https://doi.org/10.1016/j.renene.2024.120474.

[35] Wang J, Xiang Z, Huang Z, Xu Q, Yin D. Recent advances on bifunctional catalysts for one-pot conversion of furfural to γ-valerolactone. Front Chem 2022;10:959572. https://doi.org/10.3389/fchem.2022.959572.

[36] Zhu S, Xue Y, Guo J, Cen Y, Wang J, Fan W. Integrated conversion of hemicellulose and furfural into γ-valerolactone over Au/ZrO_2 catalyst combined with ZSM-5. ACS Catal 2016;6:2035–42. https://doi.org/10.1021/acscatal.5b02882.

[37] García A, Sánchez-Tovar R, Miguel PJ, Montejano-Nares E, Ivars-Barceló F, Cecilia JA, et al. Catalytic production of γ-valerolactone, a biofuel precursor, from furfural in one-pot: Synergistic effect between Zr and Sn. Fuel 2023;352:129045. https://doi.org/10.1016/j.fuel.2023.129045.

[38] Liu Z, Zhang Z, Zhou Y, Wang Z, Du M, Wen Z, et al. Phosphotungstic acid supported on Zr-SBA-15 as an efficient catalyst for one-pot conversion of furfural to γ-valerolactone. Fuel 2024;356:129631. https://doi.org/10.1016/j.fuel.2023.129631.

[39] Winoto HP, Fikri ZA, Ha J-M, Park Y-K, Lee H, Suh DJ, et al. Heteropolyacid supported on Zr-Beta zeolite as an active catalyst for one-pot transformation of furfural to γ-valerolactone. Appl Catal B Environ 2019;241:588–97. https://doi.org/10.1016/j.apcatb.2018.09.031.

[40] Li W, Li M, Liu H, Jia W, Yu X, Wang S, et al. Domino transformation of furfural to γ-valerolactone over SAPO-34 zeolite supported zirconium phosphate catalysts with tunable Lewis and Brønsted acid sites. Mol Catal 2021;506:111538. https://doi.org/10.1016/j.mcat.2021.111538.

[41] Xue W, Ma M, Hou P, Zhang P, Liu W, Liu Y, et al. One-pot tandem conversion of furfural to γ-valerolactone over a series of modified zirconium-based metal–organic frameworks with variational Lewis and Brønsted acid sites. Fuel 2024;371:132115. https://doi.org/10.1016/j.fuel.2024.132115.

[42] Maderuelo-Solera R, Richter S, Jiménez-Gómez CP, García-Sancho C, García-Mateos FJ, Rosas JM, et al. Porous SiO_2 nanospheres modified with ZrO_2 and their use in one-pot catalytic processes to obtain value-added chemicals from furfural. Ind Eng Chem Res 2021;60:18791–805. https://doi.org/10.1021/acs.iecr.1c02848.

[43] Sun W, Li H, Wang X, Liu A. Cascade upgrading of biomass-derived furfural to γ-valerolactone over Zr/Hf-based catalysts. Front Chem 2022;10:863674. https://doi.org/10.3389/fchem.2022.863674.

[44] Liu Z, Zhang Z, Fu R, Xu J, Lu J, Wen Z, et al. One-pot conversion of furfural to gamma-valerolactone over Zr-SBA-15: Cooperation of Lewis and Brønsted acidic sites. ACS Appl Nano Mater 2023;6:13196–207. https://doi.org/10.1021/acsanm.3c01845.

[45] Esposito S, Silvestri B, Rossano C, Vermile V, Imparato C, Manzoli M, et al. The role of metallic and acid sites of Ru-Nb-Si catalysts in the transformation of levulinic acid to γ-valerolactone. Appl Catal B Environ 2022;310:121340. https://doi.org/10.1016/j.apcatb.2022.121340.

[46] Hernández B, Iglesias J, Morales G, Paniagua M, López-Aguado C, Fierro JLG, et al. One-pot cascade transformation of xylose into γ-valerolactone (GVL) over bifunctional Brønsted–Lewis Zr–Al-beta zeolite. Green Chem 2016;18:5777–81. https://doi.org/10.1039/C6GC01888B.

[47] Bui L, Luo H, Gunther WR, Romμn-Leshkov Y. Domino reaction catalyzed by zeolites with Brønsted and Lewis acid sites for the production of g-valerolactone from furfural. Angew Chem Int Ed 2013;52:8022–5. https://doi.org/10.1002/anie.201302575.

[48] Wang J, Okumura K, Jaenicke S, Chuah G-K. Post-synthesized zirconium-containing Beta zeolite in Meerwein–Ponndorf–Verley reduction: pros and cons. Appl Catal A 2015;493:112–20. https://doi.org/10.1016/j.apcata.2015.01.001.

[49] Winoto HP, Ahn BS, Jae J. Production of γ-valerolactone from furfural by a single-step process using Sn-Al-Beta zeolites: Optimizing the catalyst acid properties and process conditions. J Ind Eng Chem 2016;40:62–71. https://doi.org/10.1016/j.jiec.2016.06.007.

[50] Yu Z, Lu X, Liu C, Han Y, Ji N. Synthesis of γ-valerolactone from different biomass-derived feedstocks: recent advances on reaction mechanisms and catalytic systems. Renew Sustain Energy Rev 2019;112:140–57. https://doi.org/10.1016/j.rser.2019.05.039.

[51] Zhang H, Yang W, Roslan II, Jaenicke S, Chuah G-K. A combo Zr-HY and Al-HY zeolite catalysts for the one-pot cascade transformation of biomass-derived furfural to γ-valerolactone. J Catal 2019;375:56–67. https://doi.org/10.1016/j.jcat.2019.05.020.

[52] Saotta A, Allegri A, Liuzzi F, Fornasari G, Dimitratos N, Albonetti S. Ti/Zr/O mixed oxides for the catalytic transfer hydrogenation of furfural to GVL in a liquid-phase continuous-flow reactor. Chem Engineering 2023;7:23. https://doi.org/10.3390/chemengineering7020023.

[53] García A, Saotta A, Miguel PJ, Sánchez-Tovar R, Fornasari G, Allegri A, et al. Promoter effect of Pt on Zr catalysts to increase the conversion of furfural to γ-valerolactone using batch and continuous flow reactors: Influence of the way of the incorporation of the Pt sites. Energy Fuels 2024;38:9849–61. https://doi.org/10.1021/acs.energyfuels.4c01174.
[54] García A, Monti E, Ventimiglia A, Dimitratos N, Miguel PJ, López ML, et al. Zr supported on non-acidic sepiolite for the efficient one-pot transformation of furfural into γ-valerolactone. Biomass Bioenergy 2023;170:106730. https://doi.org/10.1016/j.biombioe.2023.106730.
[55] Jehng JM, Wachs IE. Structural chemistry and Raman spectra of niobium oxides. Chem Mater 1991;3:100–7. https://doi.org/10.1021/cm00013a025.
[56] Taylor M, Ndifor EN, Garcia T, Solsona B, Carley AF, Taylor SH. Deep oxidation of propane using palladium–titania catalysts modified by niobium. Appl Catal A 2008;350:63–70. https://doi.org/10.1016/j.apcata.2008.07.045.
[57] Zholobenko V, Freitas C, Jendrlin M, Bazin P, Travert A, Thibault-Starzyk F. Probing the acid sites of zeolites with pyridine: Quantitative AGIR measurements of the molar absorption coefficients. J Catal 2020;385:52–60. https://doi.org/10.1016/j.jcat.2020.03.003.
[58] Emeis CA. Determination of integrated molar extinction coefficients for infrared absorption bands of pyridine adsorbed on solid acid catalysts. J Catal 1993;141:347–54. https://doi.org/10.1006/jcat.1993.1145.
[59] Su X-P, Zhao L, Wang X-T, Wang Z, Wang Z-C, Shen T, et al. Effect of Different Al2O3 Supports on the Synthesis of Tetralin by Selective Catalytic Hydrogenation of Naphthalene. J Braz Chem Soc 2023;34. https://doi.org/10.21577/0103-5053.20230011.
[60] Allegri A, Saotta A, Liuzzi F, Gianotti E, Paul G, Cattaneo AS, et al. Aquivion-Based Spray Freeze-Dried Composite Materials for the Cascade production of γ-Valerolactone. ChemSusChem 2024;17(14). https://doi.org/10.1002/cssc.202301683.
[61] Vlasenko NV, Kochkin YN, Telbiz GM, Shvets OV, Strizhak PE. Insight into the active site nature of zeolite H-BEA for liquid phase etherification of isobutylene with ethanol. RSC Adv 2019;9:35957–68. https://doi.org/10.1039/C9RA07721A.
[62] Ginter, DM, Bell AT, Radke CJ. Synthesis of microporous materials, Molecular Sieves 1992 Vol. 1. p. 6. M. L Occelli, H. E Robson (eds.).
[63] Treacy MMJ, Higgins JB. Collection of simulated XRD powders for zeolites. Published on behalf of the Synthesis Commission of the International Zeolite Association. Van Nostrand Reinhold, New York. 2001. Doi: 10.1016/b978-0-444-50702-0.x5000-x.
[64] Wang H, Liu GH, Li XL, Kang YH, Liu ZQ, Gao Y, et al. Catalytic hydrolysis of caragana korshinskii to valuable bio-oils over a magnetic iron niobate: combined with structural feature evaluation. ACS Sustain Resour Manage 2024;1:1573–84. https://doi.org/10.1021/acssusresmgt.4c00180.
[65] Khan M, Shaik MR, Khan ST, Adil SF, Kuniyil M, Khan M, et al. Enhanced antimicrobial activity of biofunctionalized zirconia nanoparticles. ACS Omega 2020;5:1987–96. https://doi.org/10.1021/acsomega.9b03840.
[66] Kondo JN, Hiyoshi Y, Osuga R, Ishikawa A, Wang Y-H, Yokoi T. Thin (single–triple) niobium oxide layers on mesoporous silica substrate. Microporous Mesoporous Mater 2018;262:191–8. https://doi.org/10.1016/j.micromeso.2017.11.032.
[67] Morais LA, Adán C, Araujo AS, Guedes APMA, Marugán J. Synthesis, characterization, and photonic efficiency of novel photocatalytic niobium oxide materials. Global Chall 2017;1:1700066. https://doi.org/10.1002/gch2.201700066.
[68] Milato JV, França RJ, Marques MR. Pyrolysis of oil sludge from the offshore petroleum industry: influence of different mesoporous zeolites catalysts to obtain paraffinic products. Environ Technol 2021;42:1013–22. https://doi.org/10.1080/09593330.2019.1650833.
[69] Mekki A, Benmaati A, Mokhtar A, Hachemaoui M, Zaoui F, Zahmani HH, et al. Michael addition of 1,3-dicarbonyl derivatives in the presence of zeolite Y as an heterogeneous catalyst. J Inorg Organomet Polym Mater 2019;30:2323–34. https://doi.org/10.1007/s10904-019-01424-5.
[70] Elmadani AA, Radović I, Tomić NZ, Petrović M, Stojanović DB, Heinemann RJ, et al. Hybrid denture acrylic composites with nanozirconia and electrospun polystyrene fibers. PLoS One 2019;14:e0226528. https://doi.org/10.1371/journal.pone.0226528.
[71] da Conceição LRV, Carneiro LM, Rivaldi JD, de Castro HF. Solid acid as catalyst for biodiesel production via simultaneous esterification and transesterification of macaw palm oil. Ind Crop Prod 2016;89:416–24. https://doi.org/10.1016/j.indcrop.2016.05.044.
[72] Sari EP. The FTIR image comparison of zirconium sulfate synthesis products from the pathways of Na_2ZrO_3 and zirconium oxychloride compounds. J Indian Chem Soc 2023;100:101029. https://doi.org/10.1016/j.jics.2023.101029.
[73] Weibin Z, Weidong W, Xueming W, Xinlu C, Dawei Y, Changle S, et al. The investigation of NbO2 and Nb2O5 electronic structure by XPS, UPS and first principles methods. Surf Interface Anal 2013;45:1206–10. https://doi.org/10.1002/sia.5253.
[74] Nowak A, Persson J, Schmelzer B, Szade J, Szot K. Low temperature reduction in Ta–O and Nb–O thin films. J Phys D Appl Phys 2014;47:135301. https://doi.org/10.1088/0022-3727/47/13/135301.
[75] Bagus PS, Sousa C, Illas F. XPS binding energy shifts as a function of bond distances: a case study of CO. J Phys Condens Matter 2022;34:154004. https://doi.org/10.1088/1361-648X/ac4dc0.
[76] Brenier R, Mugnier J, Mirica E. XPS study of amorphous zirconium oxide films prepared by sol–gel. Appl Surface Sci 1999;143:85–91. https://doi.org/10.1016/S0169-4332(98)00901-5.
[77] Wang J, Wang S, Peng H, Xiao Z, Xu Q, Liu X, et al. Two salicylic acid derivatives welded Zr-based hybrids relay catalysis: One-pot conversion of bio-based furfural to additive γ-valerolactone. Ind Crop Prod 2025;228:120878. https://doi.org/10.1016/j.indcrop.2025.120878.
[78] Chávez-Sifontes M, García A, Sanchis R, Furgeaud C, Mayoral A, Arenal R, et al. The promoter effect of Nb species on the catalytic performance of Ir-based catalysts for VOCs total oxidation. J Environ Chem Eng 2022;10:108261. https://doi.org/10.1016/j.jece.2022.108261.
[79] Bukhtiyarova MV, Bukhtiyarova GA. Reductive amination of levulinic acid or its derivatives to pyrrolidones over heterogeneous catalysts in the batch and continuous flow reactors: a review. Renew Sustain Energy Rev 2021;143:110876. https://doi.org/10.1016/j.rser.2021.110876.
[80] Maderuelo-Solera R, Torres-Olea B, Jiménez-Gómez CP, Moreno-Tost R, García-Sancho C, Mérida-Robles J, et al. Nb-based catalysts for the valorization of furfural into valuable product through in one-pot reaction. Int J Mol Sci 2024;25:2620. https://doi.org/10.3390/ijms25052620.
[81] Liu B, Chen X, Xu Y, Qiao C, Lu Z, Tian Y. A combo Zr–zeolite and Zr (OH) 4 mixture composition for one–pot production of γ–valerolactone from furfural. Renew Energy 2024;229:120751. https://doi.org/10.1016/j.renene.2024.120751.
[82] Iglesias J, Melero JA, Morales G, Paniagua M, Hernández B, Osatiashtiani A, et al. ZrO_2 -SBA-15 catalysts for the one-pot cascade synthesis of GVL from furfural. Cat Sci Technol 2018;8:4485–93. https://doi.org/10.1039/C8CY01121D.
[83] Duk Kim K, Kim J, Yang Teoh W, Kim J-C, Huang J, Ryoo R. Cascade reaction engineering on zirconia-supported mesoporous MFI zeolites with tunable Lewis–Brønsted acid sites: a case of the one-pot conversion of furfural to γ-valerolactone. RSC Adv 2020;10:35318–28. https://doi.org/10.1039/D0RA06915A.
[84] Byun MY, Lee MS. Pt supported on hierarchical porous carbon for furfural hydrogenation. J Ind Eng Chem 2021;104:406–15. https://doi.org/10.1016/j.jiec.2021.08.038.
[85] Byun MY, Eun Kim Y, Ho Baek J, Jae J, Sig LM. Effect of surface properties of TiO_2 on the performance of Pt/TiO_2 catalysts for furfural hydrogenation. RSC Adv 2022;12:860–8. https://doi.org/10.1039/D1RA07220J.